

---

# DEFORMTIME: Capturing Variable Dependencies with Deformable Attention for Time Series Forecasting

---

**Yuxuan Shu**

Department of Computer Science  
University College London, UK  
yuxuan.shu.22@ucl.ac.uk

**Vasileios Lamos**

Department of Computer Science  
University College London, UK  
v.lamos@ucl.ac.uk

## Abstract

In multivariate time series (MTS) forecasting, existing state-of-the-art deep learning approaches tend to focus on autoregressive formulations and overlook the information within exogenous indicators. To address this limitation, we present DEFORMTIME,<sup>1</sup> a neural network architecture that attempts to capture correlated temporal patterns from the input space, and hence, improve forecasting accuracy. It deploys two core operations performed by deformable attention blocks (DABs): learning dependencies across variables from different time steps (variable DAB), and preserving temporal dependencies in data from previous time steps (temporal DAB). Input data transformation is explicitly designed to enhance learning from the deformed series of information while passing through a DAB. We conduct extensive experiments on 6 MTS data sets, using previously established benchmarks as well as challenging infectious disease modelling tasks with more exogenous variables. The results demonstrate that DEFORMTIME improves accuracy against previous competitive methods across the vast majority of MTS forecasting tasks, reducing the mean absolute error by 10% on average. Notably, performance gains remain consistent across longer forecasting horizons.

## 1 Introduction

Time series forecasting models provide multifaceted solutions for many application domains, including health [15, 39], climate [37], energy [7], transport [24], and finance [38]. In their pursuit for greater accuracy, forecasting methods have always been trying to benefit from multimodal exogenous predictors [1, 6]. Over recent years, a plethora of new digitised information sources has become available, accompanied by a rapid development of capable and efficient deep learning architectures [19, 35]. However, current state-of-the-art (SOTA) models for multivariate time series (MTS) forecasting favour the deployment of many-to-many sequence deep learning architectures [29, 32, 44, 46]. We argue that this modelling approach does not necessarily provide the right learning mechanism for tasks with a definitive target (endogenous) variable and a considerable amount of exogenous variables. Furthermore, although various neural networks (NNs) were proposed to address MTS forecasting challenges [13, 29, 51, 55], many [16, 17, 23, 32, 53] were not designed to incorporate inter-variate dependencies, a key property of conventional forecasters [3, 14, 34].

There certainly exist neural MTS forecasting models that attempt to leverage dependencies across variables and time. Solutions based on recurrent neural network (RNN) architectures [19, 25] can capture information from previous time steps (up to an extent), but have a limited capacity in establishing inter-variate dependencies. LightTS [54] uses multi-layer perceptrons to model dependencies within the input data, first along the temporal dimension and then across variables. For transformer-based models, Crossformer [55] proposes to first partition the input into temporal

---

<sup>1</sup>The source code of DEFORMTIME is available at [github.com/ClaudiaShu/DeformTime](https://github.com/ClaudiaShu/DeformTime).

patches, and then use a router module to capture information across variables from different time steps, improving performance compared to pre-established RNN and Graph NN architectures [19, 47]. However, both LightTS and Crossformer have been outperformed by later proposed models that do not establish dependencies between variables [16, 17, 23, 32, 53]. The counterargument from these approaches is that forecasters without inter-variable dependency modules benefit from being able to use longer look-back windows without significantly increasing model complexity [11]. Nevertheless, a common issue throughout the deep learning MTS forecasting literature that casts doubt on some of these conclusions is the inappropriateness of various benchmark tasks (see Appendix A.5). In addition, recent work has argued that to improve performance while exploiting inter-variable dependencies, more effort is required in temporally aligning the input time series [56]. Motivated by this, we have introduced guided re-arrangements of the input to better capture inter- and intra-variable dynamics.

Deformable neural networks were initially proposed in computer vision [5] to accommodate geometric transformations with Convolutional Neural Networks (CNNs). Combined with transformer-based NN architectures, deformation has achieved SOTA performance in various tasks [4, 48, 60]. Combining our aforementioned insights with the concept of deformation has led to the development of DEFORMTIME, a novel MTS forecasting model that deploys a deformable module on top of transformer encoders to introduce some flexibility in the determination of receptive fields across different variables and time steps. The premise of DEFORMTIME is the inclusion of learnable mechanisms that we refer to as deformable attention blocks (DABs). These enable transformations of the input information stream that enhance learning from key patterns within endo- but most importantly exogenous variables, an operation that ultimately improves forecasting accuracy.

We summarise the main contributions of this paper as follows:

- (a) We propose DEFORMTIME, a novel MTS forecasting model, that better captures inter- and intra-variate dependencies at different temporal granularities. It comprises two DABs which facilitate learning from adaptively transformed input across variables (V-DAB) and time (T-DAB).
- (b) We assess the predictive accuracy of MTS forecasters on 3 established benchmarks as well as 3 new infectious disease prevalence tasks, each across 4 increasing horizons. We argue that the disease prevalence tasks support a more thorough evaluation because data sets include a substantial amount of exogenous variables, and encompass multiple years, 4 of which are used as distinct annual test periods.
- (c) In our experiments, DEFORMTIME reduces the mean absolute error (MAE) by 10% on average compared to the most competitive forecasting method (can be a different one each time). There is a 7.4% MAE reduction based on established benchmarks and 12.6% for the disease forecasting tasks. Overall, performance gains remain stable as the forecasting horizon increases.
- (d) As an aside, we note that models that attempt to establish some form of inter-variable dependency performed better in evidently (based on the results) the more challenging task of disease forecasting. This also highlights the need for more appropriate methods of assessment.

## 2 MTS forecasting task definition

Across our experiments, we consider an MTS forecasting task where the focus is on a single target variable, i.e. there might exist multiple inputs, and optionally multiple outputs, but we are only concerned with the predictions of one output variable. All models follow a rolling window forecasting setting with a look-back window of  $L$  time steps. To be more precise, at time step  $t$ ,  $\mathbf{Q}_t \in \mathbb{R}^{L \times C}$  holds the time series of  $C$  exogenous variables over the  $L$  time steps  $\{t-L+1, \dots, t-1, t\}$ . In addition,  $\mathbf{y}_{t-\delta} \in \mathbb{R}^L$  holds the corresponding  $L$  autoregressive historical values for the target variable for time steps  $\{t-\delta-L+1, \dots, t-\delta-1, t-\delta\}$ . Note that  $\delta \in \mathbb{N}_0$  introduces an optional delay of  $\delta$  time steps between the observed exogenous variables and the endogenous (target) variable. This becomes relevant in a real-time infectious disease forecasting task, where estimates for the rate of an infectious disease are becoming available with a delay of  $\delta = 7$  or 14 days, when other indicators are not affected by this (see Appendix A.2). Joining both input signals, we obtain  $\mathbf{Z}_t = [\mathbf{Q}_t, \mathbf{y}_{t-\delta}] \in \mathbb{R}^{L \times (C+1)}$ . Commonly, the prediction target is denoted by  $\mathbf{y}_{t+H} \in \mathbb{R}^H$ , where  $H$  indicates the number of time steps we are forecasting ahead. However, some (baseline) models follow a multi-task learning formulation whereby every input variable becomes a prediction target. On this occasion, the prediction targets are denoted by  $\mathbf{Y}_{t+H} = [\mathbf{Q}_{t+H}, \mathbf{y}_{t+H}] \in \mathbb{R}^{H \times (C+1)}$ . Hence, the aim of the forecasting task is to learn a function  $f(\cdot)$  such that  $f: \mathbf{Z}_t \rightarrow \mathbf{y}_{t+H}$  or  $\mathbf{Y}_{t+H}$ . Irrespective

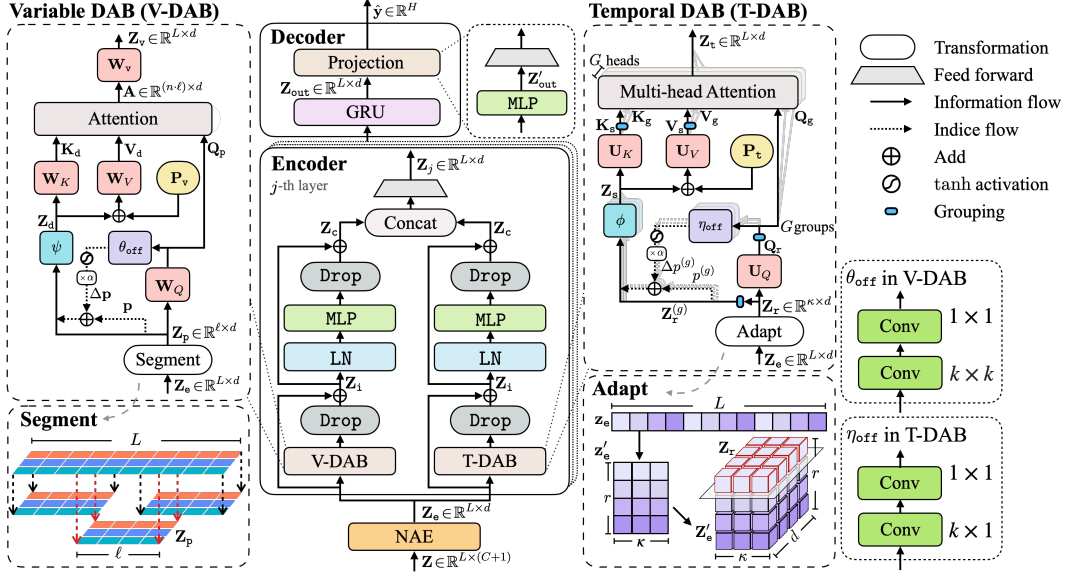


Figure 1: The architecture of DEFORMTIME. We use the notation introduced in sections 2 and 3. DEFORMTIME’s core modules comprise two deformable attention blocks (DABs), a variable DAB (V-DAB) and a temporal DAB (T-DAB) that respectively capture inter- and intra-variable dependencies. Both DABs reside in the **Encoder** module. We deploy a 2-layer GRU as the **Decoder**. Finally, we have visualised key data operations (**Segment** and **Adapt** blocks) that take place in the DABs.

of the number of outputs, forecasting accuracy is reported on the final estimate of  $\mathbf{y}_{t+H}$ ,  $y_{t+H} \in \mathbb{R}$ , which denotes the value of the target variable at time step  $t+H$ . For notational simplicity, we have chosen to only imply temporal subscripts for the remainder of the manuscript (i.e. use  $\mathbf{Z}$  over  $\mathbf{Z}_t$ ).

### 3 Time series forecasting with DEFORMTIME

An overview of DEFORMTIME’s structure is presented in Figure 1. Motivated by our assumption that variables (endo- and exogenous) in an MTS task may not only be correlated with the historical values of the target variable, but also with other predictors within adjacent time steps, DEFORMTIME deploys a modified transformer encoder layer with two core modules that attempt to account for both dependencies: a Variable Deformable Attention Block (V-DAB) to capture inter-variable dependencies across time, and a Temporal Deformable Attention Block (T-DAB) to capture intra-variable dependencies across different time periods. In the following sections, we provide a detailed description of all modules and operations of DEFORMTIME.

#### 3.1 Multi-head attention

We first revisit the multi-head attention mechanism originally proposed by Vaswani et al. [41]. Given an input  $\mathbf{Z} \in \mathbb{R}^{v \times u}$ ,  $\mathbf{Q}$ ,  $\mathbf{K}$ , and  $\mathbf{V} \in \mathbb{R}^{v \times u}$  respectively denote the query, key, and value embeddings projected from  $\mathbf{Z}$  with learnable linear projection matrices  $\mathbf{W}_Q$ ,  $\mathbf{W}_K$ , and  $\mathbf{W}_V \in \mathbb{R}^{u \times u}$  (as in  $\mathbf{Q} = \mathbf{Z}\mathbf{W}_Q$ ). Assuming  $M$  attention heads, these embeddings are each partitioned into  $M$  non-overlapping submatrices column-wise. For example, the  $m$ -th submatrix of  $\mathbf{Q}$ , denoted by  $\mathbf{Q}_m$ , has a dimensionality of  $v \times (u/M)$ . Following up on this notational convention, the output of the  $m$ -th attention head,  $\mathbf{A}_m \in \mathbb{R}^{v \times (u/M)}$ , is given by

$$\mathbf{A}_m = \text{softmax}\left(\mathbf{Q}_m \mathbf{K}_m^\top / \sqrt{u/M}\right) \mathbf{V}_m. \quad (1)$$

The outputs from each head are then concatenated along the second dimension and linearly projected into the hidden dimension  $u$  with a weight matrix  $\mathbf{W} \in \mathbb{R}^{u \times u}$  to form the output  $\mathbf{A} \in \mathbb{R}^{v \times u}$ . When we set  $M = 1$ , we refer to this method as single-head attention.

### 3.2 Neighbourhood-aware input embedding

The receptive field of DEFORMTIME is determined by a CNN with sampling offset (see section 3.3). This introduces a limitation in capturing relationships between neighbouring variables. We seek to minimise the impact of this by learning a Neighbourhood-Aware input Embedding (NAE) as follows. We first re-arrange the order of variables in the input  $\mathbf{Z}$ , ranking them based on their linear correlation with the target variable in a temporally aligned fashion (see also Appendix C.1). We then embed the correlation-driven re-arranged version of the input that captures  $C + 1$  variables to a hidden dimension  $d$ . However, we do not perform this embedding as a single holistic step, but embed  $G$  neighbouring groups of variables, each one to a shortened embedding of size  $d/G$ , using a fully connected layer.<sup>2</sup> Both  $d$  and  $G$  are hyperparameters that we learn during training. The embeddings of each input variable grouping are concatenated to form  $\mathbf{E} \in \mathbb{R}^{L \times d}$ . Finally, we also add a sinusoidal position embedding [41, 57],  $\mathbf{P}_n \in \mathbb{R}^{L \times d}$ , to  $\mathbf{E}$ , and normalise within layer as widely adopted in prior work [8, 55]. Hence, the embedding  $\mathbf{Z}_e \in \mathbb{R}^{L \times d}$  of the input  $\mathbf{Z}$  is given by

$$\mathbf{Z}_e = \text{LN}(\mathbf{E} + \mathbf{P}_n) , \quad (2)$$

where  $\text{LN}(\cdot)$  denotes layer normalisation [2].

### 3.3 Variable deformable attention block (V-DAB)

The embedded input sequence,  $\mathbf{Z}_e$ , is first segmented into patches along the temporal dimension that encompasses a total of  $L$  time steps. By deploying a segmentation length  $\ell$  and a stride  $s \leq \ell$  (to ensure all data points are included), we obtain  $n = \lfloor (L - \ell) / s \rfloor + 1$  patches, denoted by  $\mathbf{Z}_p \in \mathbb{R}^{\ell \times d}$ .<sup>3</sup> We augment the vanilla Transformer attention [41] with a deformable mechanism which allows the network to adaptively attend across time and variables. Each data point in a patch  $\mathbf{Z}_p$  can be represented by a pair of (row, column) indices,  $\mathbf{p} = (i, j)$ . We sample from a deformed position  $\mathbf{p} + \Delta\mathbf{p}$  over  $\mathbf{Z}_p$  to obtain the key and value embeddings,  $\mathbf{K}_d, \mathbf{V}_d \in \mathbb{R}^{\ell \times d}$ , respectively.

To determine the offset  $\Delta\mathbf{p} \in \mathbb{R}^2$  we conduct the following series of operations. We first obtain a query embedding,  $\mathbf{Q}_p \in \mathbb{R}^{\ell \times d}$ , over a patch of the input as described in section 3.1, i.e.  $\mathbf{Q}_p = \mathbf{Z}_p \mathbf{W}_Q$ . We then pass  $\mathbf{Q}_p$  from a 2D CNN, denoted by  $\theta_{\text{off}}$ , comprising a convolutional layer with a  $k \times k$  kernel that captures neighbouring information, and a  $1 \times 1$  convolutional layer that projects the embedded feature. We use the tanh activation function and a learnable amplitude  $\alpha \in \mathbb{R}_{>0}$  (that controls the upper bound of the sampling range) to obtain  $\Delta\mathbf{p}$ . Hence,  $\Delta\mathbf{p}$  is given by

$$\Delta\mathbf{p} = \alpha \cdot \tanh(\theta_{\text{off}}(\mathbf{Q}_p)) . \quad (3)$$

We use  $\Delta\mathbf{p}$  and bilinear interpolation ( $\psi$ ) over a  $2 \times 2$  grid determined by  $\mathbf{p} + \Delta\mathbf{p}$  [5], to obtain the deformed patch  $\mathbf{Z}_d$ :

$$\mathbf{Z}_d = \psi(\mathbf{Z}_p; \mathbf{p} + \Delta\mathbf{p}) .^4 \quad (4)$$

We then obtain  $\mathbf{K}_d, \mathbf{V}_d$  from  $\mathbf{Z}_d$  with

$$\mathbf{K}_d = \mathbf{Z}_d \mathbf{W}_K \quad \text{and} \quad \mathbf{V}_d = \mathbf{Z}_d \mathbf{W}_V + \mathbf{P}_v , \quad (5)$$

where  $\mathbf{P}_v \in \mathbb{R}^{\ell \times d}$  is a relative positional bias [40] that is added to assist in maintaining some pairwise positional information after the deformation.

A single head self-attention layer is applied to attend  $\mathbf{Q}_p$  to  $\mathbf{K}_d, \mathbf{V}_d$  given by

$$\mathbf{A}_i = \left( \text{softmax}\left(\mathbf{Q}_p \mathbf{K}_d^\top / \sqrt{d}\right) \mathbf{V}_d \right) \mathbf{W}_i , \quad (6)$$

where  $\mathbf{W}_i \in \mathbb{R}^{d \times d}$  is the weight matrix, to form the attention embedding  $\mathbf{A}_i \in \mathbb{R}^{\ell \times d}$  for the  $i$ -th segmented patch. The output from all patches is concatenated across the temporal dimension, forming  $\mathbf{A} \in \mathbb{R}^{(n \cdot \ell) \times d}$ . The final output of the V-DAB module,  $\mathbf{Z}_v \in \mathbb{R}^{L \times d}$ , is given by

$$\mathbf{Z}_v = \mathbf{W}_v^\top \mathbf{A} , \quad (7)$$

where  $\mathbf{W}_v \in \mathbb{R}^{(n \cdot \ell) \times L}$  denotes the weight matrix of a fully connected layer.

<sup>2</sup>The input is zero-padded to a proper length, if the number of variables is not divisible by  $G$ .

<sup>3</sup> $\mathbf{Z}_e$  is zero-padded into proper length, if  $L - \ell$  not divisible by  $s$ .

<sup>4</sup>If a sampling position is out-of-bounds, we interpolate using zero values.

### 3.4 Temporal deformable attention block (T-DAB)

The T-DAB module receives the same input as the V-DAB module ( $\mathbf{Z}_e$ ). Based on insights from prior work [16, 46], we first adapt  $\mathbf{Z}_e$  to support learning from different temporal resolutions. Specifically, every column  $\mathbf{z}_e \in \mathbb{R}^L$  of  $\mathbf{Z}_e$  is transformed to  $\mathbf{z}'_e \in \mathbb{R}^{r \times \kappa}$ , where  $r$  denotes the time window (amount of time steps) that T-DAB is using for capturing temporal relationships, and  $\kappa = L/r$ .<sup>5</sup> This converts a vector representing  $L$  time steps,  $\{t_1, t_2, \dots, t_L\}$ , to an  $r \times \kappa$  matrix where the starting time for each row is  $\{t_1, t_2, \dots, t_r\}$ , and the time stamps for the elements of the  $j$ -th row are  $\{t_j, t_{j+r}, t_{j+2r}, \dots, t_{j+(\kappa-1)r}\}$ . Therefore,  $\mathbf{Z}_e$  becomes  $\mathbf{Z}'_e \in \mathbb{R}^{r \times \kappa \times d}$ , which comprises  $r$  patches; a patch for T-DAB is denoted by  $\mathbf{Z}_r \in \mathbb{R}^{\kappa \times d}$ .

The factor  $r$  (time steps) can be set to different values across encoder layers to capture dependencies at various temporal granularities (see Appendix C). If we set  $r = 1$ ,  $\mathbf{Z}_e$  remains unchanged. Similarly to V-DAB, we obtain the query embedding  $\mathbf{Q}_r \in \mathbb{R}^{\kappa \times d}$  over the transformed input using  $\mathbf{Q}_r = \mathbf{Z}_r \mathbf{U}_Q$ , where  $\mathbf{U}_Q \in \mathbb{R}^{d \times d}$  is a weight matrix. We then implement an augmented Transformer attention that contains deformed information across the temporal dimension. We work our way column-wise, and for every column  $\mathbf{z}_r \in \mathbf{Z}_r$ , we sample (linearly as opposed to the bilinear approach in V-DAB) from an index position  $p + \Delta p \in \mathbb{R}$ .

The position offset ( $\Delta p$ ) is shared among groups of correlated embedded sequences as they may have similar temporal dependencies. Given that the original input variables were already grouped based on their correlation with the target signal (section 3.2), we expect that correlations are already captured in feature neighbourhoods of  $\mathbf{Z}_r$ . Therefore, to obtain  $\Delta p$ , we first divide  $\mathbf{Q}_r$  into the same  $G$  subgroups (column-wise) as in the NAE operation. Each subgroup,  $\mathbf{Q}_g \in \mathbb{R}^{\kappa \times (d/G)}$  with  $g = \{1, \dots, G\}$ , shares the same temporal deformation controlled by  $\Delta p^{(g)}$ . Similarly to Eq. 3,  $\Delta p^{(g)}$  is defined as

$$\Delta p^{(g)} = \alpha \cdot \tanh(\eta_{\text{off}}(\mathbf{Q}_g)), \quad (8)$$

with  $\eta_{\text{off}}$  denoting a 1D CNN (with a  $k \times 1$  and  $1 \times 1$  convolution layers), and  $\alpha$  being the same offset amplitude as in V-DAB. We then obtain the matrix of temporally deformed sequences  $\mathbf{Z}_s = [\mathbf{Z}_s^{(1)}, \dots, \mathbf{Z}_s^{(G)}] \in \mathbb{R}^{\kappa \times d}$ ; each submatrix,  $\mathbf{Z}_s^{(g)} \in \mathbb{R}^{\kappa \times (d/G)}$ , is given by

$$\mathbf{Z}_s^{(g)} = \phi(\mathbf{z}_r \in \mathbf{Z}_r^{(g)}; p + \Delta p^{(g)}), \quad (9)$$

where  $\phi(\cdot)$  denotes a linear interpolation function over 2 adjacent points of  $\mathbf{z}_r \in \mathbf{Z}_r^{(g)}$  determined by the deformed index  $p + \Delta p^{(g)}$ .

Similarly to V-DAB,  $\mathbf{K}_s, \mathbf{V}_s \in \mathbb{R}^{\kappa \times d}$  are obtained from  $\mathbf{Z}_s$ , using  $\mathbf{K}_s = \mathbf{Z}_s \mathbf{U}_K$ , and  $\mathbf{V}_s = \mathbf{Z}_s \mathbf{U}_V + \mathbf{P}_t$ , where  $\mathbf{P}_t \in \mathbb{R}^{\kappa \times d}$  is a relative positional bias. We then apply multi-head attention, by first splitting  $\mathbf{K}_s$  and  $\mathbf{V}_s$  into  $G$  groups (submatrices) denoted by  $\mathbf{K}_g$  and  $\mathbf{V}_g \in \mathbb{R}^{\kappa \times (d/G)}$ , and then by using  $\mathbf{A}_g = \text{softmax}(\mathbf{Q}_g \mathbf{K}_g^T / \sqrt{d/G}) \mathbf{V}_g$ . The outputs from different heads are concatenated column-wise and linearly projected with a weight matrix  $\mathbf{W}_i \in \mathbb{R}^{d \times d}$  to obtain the attention embedding of the  $i$ -th patch  $\mathbf{A}_i \in \mathbb{R}^{\kappa \times d}$ . To form the output of T-DAB, denoted by  $\mathbf{Z}_t \in \mathbb{R}^{L \times d}$ , the outputs of all patches are concatenated along the first dimension and re-arranged back to the original temporal structure (matching the input  $\mathbf{Z}_e$  as well as V-DAB's output  $\mathbf{Z}_v$ ).

### 3.5 Encoder

The encoder of DEFORMTIME may consist of more than one layer. In our experiments, we deploy 2 encoder layers, similarly to related work [28, 46]. Each encoder layer contains two DAB branches (on the left and right side, respectively – see also Figure 1), comprising stacked transformer blocks [8] with layer normalisation placed within the residual connection [48, 49]. Instead of using vanilla attention, we are introducing a V-DAB (left side) and a T-DAB (right side) module to capture inter- and intra-variate dependencies, respectively. The operations of a branch can be summarised by

$$\mathbf{Z}_i = \text{Drop}(\text{DAB}(\mathbf{Z}_e)) + \mathbf{Z}_e \text{ followed by } \mathbf{Z}_c = \text{Drop}(\text{MLP}(\text{LN}(\mathbf{Z}_i))) + \mathbf{Z}_e, \quad (10)$$

where  $\text{DAB}(\cdot)$  denotes the V-DAB or T-DAB operation,  $\mathbf{Z}_i, \mathbf{Z}_c \in \mathbb{R}^{L \times d}$  are an intermediate output and the output of the DAB encoder layer, respectively,  $\text{Drop}(\cdot)$  denotes stochastic depth [12] where

<sup>5</sup> $\mathbf{z}'_e$  is padded to a proper length with the last available value, if  $L$  is not divisible by  $r$ .



layers within the network are randomly dropped during training with a learnable probability, and  $\text{MLP}(\cdot)$  is a 2-layer perceptron with ReLU activation and a hidden size of  $d$ . The outputs from the two encoder branches are concatenated over the second dimension. We feed the concatenated output into a fully connected layer to form the output  $\mathbf{Z}_j \in \mathbb{R}^{L \times d}$  of the  $j$ -th encoder layer.

### 3.6 Encoder-decoder structure

In T-DAB (section 3.4), we set the time window  $r$  to different values across encoder layers, enabling the model to attend to information at multiple temporal granularities. To effectively learn from this encoding, we construct a hierarchical encoder structure motivated by prior related work [26, 55, 57]. Specifically, the output from encoder layer  $j-1$ ,  $\mathbf{Z}_{j-1} \in \mathbb{R}^{L \times d}$ , becomes the input to encoder layer  $j$ . This is formulated by

$$\mathbf{Z}_j = \begin{cases} \text{Enc}(\mathbf{Z}_c) & \text{if } j = 1 \\ \text{Enc}(\mathbf{Z}_{j-1}) & \text{otherwise} \end{cases}, \quad (11)$$

where  $\text{Enc}(\cdot)$  denotes the operations of an encoder layer with deformable attention (section 3.5). The output of the final encoder layer is fed to a 2-layer Gated Recurrent Unit (GRU) NN with a hidden dimension of  $d$  that acts as the decoder. The output of the GRU decoder,  $\mathbf{Z}_{\text{out}}$ , maintains the same dimensionality as the input, i.e.  $L \times d$ . Finally, we use a 2-layer perceptron with a hidden dimension of  $d$  and LeakyReLU activation to project  $\mathbf{Z}_{\text{out}}$  along the temporal dimension, forming an intermediate output  $\mathbf{Z}'_{\text{out}} \in \mathbb{R}^{H \times d}$ , where  $H$  denotes the number of steps we are forecasting ahead as defined in section 2. We then feed  $\mathbf{Z}'_{\text{out}}$  to a fully connected layer to linearly project it into the target forecasting output  $\hat{y} \in \mathbb{R}^H$ .

## 4 Results

We present forecasting accuracy results across 3 benchmark and 3 disease rate prediction tasks, comparing DEFORMTIME to other competitive ‘baseline’ models. In addition, we provide an ablation study and a computational complexity / efficiency analysis.

### 4.1 Forecasting tasks, baseline methods, and experiment settings

Experiments are conducted on 6 real-world data sets. These include 3 established benchmarks from previously published papers [29, 32, 45, 46, 52, 53], namely a weather and 2 electricity transformer temperature (ETTh1 and ETTh2) tasks with respective temporal resolutions of 10 minutes and 1 hour. In addition, we have formed 3 disease rate modelling tasks, focusing on the prediction of influenza-like illness (ILI) rates in England (ILI-ENG) and US Health & Human Services (HHS) Regions 2 and 9 (ILI-US2 and ILI-US9). For the ILI rate forecasting tasks, we also introduce the frequency time series of web searches as exogenous predictors. In the ETT and weather tasks, we consider oil and wet-bulb temperature, respectively, as the target variables; we refer to the rest indicators as exogenous variables. We note that the ILI forecasting tasks have considerably more exogenous variables compared to the ETTh1, ETTh2, and weather tasks. Based on the evaluation settings in prior work [28, 32], for the ETT and weather tasks, we set the forecasting horizon  $H$  to 96, 192, 336, and 720 time steps, and use a single test fold of consecutive unseen instances. For the ILI forecasting task, we conduct experiments on 4 consecutive influenza seasons (2015/16 to 2018/19) as separate test sets (4 test folds); the forecasting horizons we consider are  $H = \{7, 14, 21, 28\}$  days ahead. Further details, including the evaluation setup are available in Appendix A.

We compare DEFORMTIME to 6 competitive forecasting models that were initially designed for MTS tasks and, to the best of our knowledge, form the current SOTA methods. These are LightTS [54], DLinear [53], Crossformer [55], PatchTST [32], iTransformer [28], and TimeMixer [44]. We also include a naïve persistence model baseline (Appendix B). For the ILI forecasting tasks, we conduct hyperparameter tuning for all models. In the benchmark tasks, with the exception of Crossformer and LightTS, we adopt the settings from their official repositories to reproduce results. Further details about the experiment settings can be found in Appendix C.

Table 1: Forecasting accuracy results across all tasks and methods.  $H$  denotes the forecasting horizon time steps. For the ILI forecasting tasks, the table enumerates the average error across the 4 test seasons. Complete results per season are shown in Appendix D.  $\epsilon$  % denotes sMAPE (to reduce column width). The best results are in **bold** font and the second best are underlined.

Models	DEFORMTIME		PatchTST		iTransformer		TimeMixer		Crossformer		LightTS		DLinear		Persistence		
	$H$	MAE	$\epsilon$ %	MAE	$\epsilon$ %	MAE	$\epsilon$ %	MAE	$\epsilon$ %	MAE	$\epsilon$ %	MAE	$\epsilon$ %	MAE	$\epsilon$ %	MAE	$\epsilon$ %
ETT1	96	<b>0.1941</b>	<b>14.96</b>	<u>0.2017</u>	<u>15.41</u>	0.2052	15.46	0.2112	16.32	0.2126	16.52	0.2215	17.24	0.2599	20.82	0.2371	18.47
	192	<b>0.2116</b>	<b>16.08</b>	0.2409	18.29	0.2429	18.13	<u>0.2382</u>	<u>17.91</u>	0.2820	21.63	0.2636	20.55	0.3798	31.78	0.2803	21.46
	336	<b>0.2158</b>	<b>16.27</b>	<u>0.2559</u>	19.29	0.2593	<u>19.11</u>	0.2625	19.72	0.2947	22.65	0.2807	22.15	0.6328	58.34	0.3028	22.90
	720	<b>0.2862</b>	<b>21.81</b>	0.3087	23.89	<u>0.2886</u>	<u>22.05</u>	0.3055	23.25	0.3350	24.84	0.5334	44.57	0.7563	69.52	0.3222	25.29
ETT2	96	<b>0.3121</b>	<u>40.07</u>	<u>0.3145</u>	<b>39.25</b>	0.3420	42.41	0.3454	41.27	0.3486	40.71	0.3507	41.80	0.3349	41.68	0.3522	43.85
	192	<b>0.3281</b>	<b>37.90</b>	0.3839	45.45	0.4233	47.44	0.4183	47.49	0.4035	43.16	0.4022	48.01	0.4084	50.67	0.4416	50.24
	336	<b>0.3450</b>	<b>37.00</b>	<u>0.4018</u>	46.77	0.4332	<u>45.95</u>	0.4380	46.79	0.4487	49.44	0.4425	51.35	0.4710	55.53	0.4836	53.70
	720	<b>0.3640</b>	<b>34.99</b>	0.4960	55.27	<u>0.4565</u>	<u>45.40</u>	0.4729	46.37	0.5832	61.45	0.6252	70.50	0.7981	94.67	0.5199	58.75
Weather	96	<b>0.0244</b>	<b>37.89</b>	0.0258	39.37	0.0277	42.39	0.0322	45.90	0.0271	44.92	0.0293	48.48	<u>0.0251</u>	<u>39.03</u>	0.0329	51.83
	192	<b>0.0260</b>	<b>39.33</b>	0.0279	<u>42.02</u>	0.0277	42.77	0.0347	48.62	0.0308	54.14	0.0319	51.45	<u>0.0270</u>	42.68	0.0361	54.92
	336	<b>0.0291</b>	<b>44.26</b>	0.0303	<u>45.31</u>	0.0308	46.01	0.0359	49.75	0.0345	62.53	0.0317	50.83	0.0305	47.68	0.0361	55.14
	720	<u>0.0363</u>	<b>53.72</b>	0.0389	56.04	0.0395	57.01	0.0457	59.82	0.0395	65.47	0.0386	62.96	<b>0.0352</b>	<u>54.54</u>	0.0394	56.04
ILI-ENG	7	<b>1.6417</b>	28.61	2.3115	27.61	2.3084	26.38	2.1748	25.68	1.8698	25.71	2.2397	52.25	2.8214	43.02	2.1710	<b>24.96</b>
	14	<b>2.2308</b>	33.98	3.2547	37.76	3.2301	36.67	3.0209	35.39	<u>2.6543</u>	<b>30.97</b>	2.6879	38.29	3.7922	55.28	3.0625	<u>33.77</u>
	21	<b>2.6500</b>	<b>32.70</b>	4.3192	51.11	4.2347	48.93	3.5501	49.36	<u>3.0014</u>	<u>40.57</u>	3.3616	51.78	4.4739	61.25	3.8617	42.03
	28	<b>2.7228</b>	<b>40.44</b>	4.9964	59.60	4.8125	55.35	4.1188	54.60	<u>3.1983</u>	<u>46.14</u>	3.4132	55.59	5.0347	67.75	4.5857	49.49
ILI-US2	7	<b>0.4122</b>	<b>16.01</b>	0.7097	24.52	0.6507	23.24	0.5284	20.07	<u>0.4400</u>	<u>16.46</u>	0.4632	16.74	0.7355	27.94	0.6474	22.48
	14	<b>0.4752</b>	<b>17.73</b>	0.8635	30.11	0.7896	28.17	0.6556	24.61	0.5852	<u>20.98</u>	<u>0.5827</u>	23.11	0.8435	32.22	0.8135	28.24
	21	<b>0.5425</b>	<b>22.13</b>	1.0286	36.70	0.8042	30.03	0.6794	27.68	<u>0.6245</u>	<u>22.29</u>	0.6683	29.27	0.9124	34.93	0.9635	33.51
	28	<b>0.5538</b>	<b>22.25</b>	1.1525	42.61	0.9619	36.75	0.8853	36.53	<u>0.6512</u>	<u>23.91</u>	0.7175	27.73	0.9805	37.62	1.1007	38.54
ILI-US9	7	<b>0.2622</b>	<b>12.26</b>	0.4116	19.34	0.4057	18.57	0.3239	15.21	<u>0.3149</u>	<u>14.44</u>	0.3185	15.65	0.4675	23.47	0.4057	18.49
	14	<b>0.3084</b>	<b>13.80</b>	0.5020	24.09	0.4702	22.44	0.4060	19.08	<u>0.3571</u>	<u>17.23</u>	0.3791	19.04	0.5467	27.35	0.5008	23.07
	21	<b>0.3179</b>	<b>14.24</b>	0.5935	29.40	0.5106	24.11	0.4576	21.40	<u>0.3418</u>	<u>15.90</u>	0.4754	23.74	0.6001	29.66	0.5906	27.41
	28	<b>0.3532</b>	<b>15.74</b>	0.6665	33.35	0.6498	31.04	0.5124	24.11	<u>0.3747</u>	<u>16.44</u>	0.4769	23.22	0.6564	32.16	0.6799	31.67

## 4.2 Forecasting accuracy

Forecasting accuracy for all tasks, models, and horizons is enumerated in Table 1. Mean Absolute Error (MAE) and symmetric Mean Absolute Percentage of Error (sMAPE<sup>6</sup> or  $\epsilon$  %) are used as our evaluation metrics. Note that for the ILI rate prediction tasks, the error metrics represent the average MAE and sMAPE across 4 consecutive test seasons (per season results are available in Tables D1, D2, and D3, including linear correlation with the target variable as an additional metric), whereas for the remaining benchmark tasks performance metrics are obtained from one train / test split for each forecasting horizon, following previously reported evaluations.

DEFORMTIME displays an overall superior accuracy. It outperforms the most competitive method (that might be a different one per task and horizon), reducing its MAE by 10% and its sMAPE by 7.4% on average across all tasks and forecasting horizons. In more absolute terms, DEFORMTIME is the best performing model in all but one occasion (where it is the second best) based on MAE, and 21 out of 24 times based on sMAPE. With the exception of the weather task that draws upon a 1-year data set from a single location and hence is only expected to offer limited insights while attempting to predict 720 time steps (7.5 days) ahead (see also Appendix A.5), our method offers >10% of MAE reduction in the most challenging forecasting tasks. Specifically, MAE is reduced by 10.5% in the ETT tasks (for  $H = 720$  hours), and by 14.9% (England) or 10.3% (US Regions) in the ILI tasks (for  $H = 28$  days). Therefore, performance gains do not decrease as the forecasting horizon increases.

When comparing DEFORMTIME to a specific forecaster, we notice that MAE reduction is >15% on average across all tasks and forecasting horizons, ranging from a 15.2% reduction vs. Crossformer to 34.8% vs. DLinear.<sup>7</sup> These significant performance gains highlight our model’s capacity to consistently perform well under different tasks and horizons compared to other SOTA models. Interestingly, DLinear fails to surpass the average accuracy of a naïve persistence model (DEFORMTIME reduces persistence’s MAE by 30.1%).

<sup>6</sup>sMAPE (Appendix D.1) can provide balanced insights when metrics are averaged across different tasks.

<sup>7</sup>A brief note to further explain DLinear’s performance is provided in Appendix D.6.

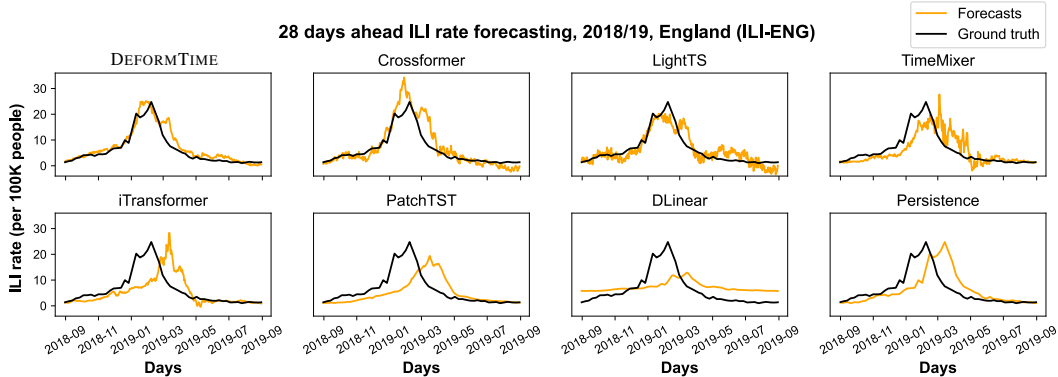


Figure 2: 28 days ahead forecasting results for influenza season 2018/19 in England (ILI-ENG) for all models. The black line denotes the ground truth, i.e. the reported (actual) ILI rates.

Turning our focus to the more interpretable task of predicting ILI rates, we first notice that forecasters that model inter-variable dependencies (Crossformer, LightTS, TimeMixer, iTransformer, and DEFORMTIME) showcase superior performance. Compared to DEFORMTIME’s average sMAPE (across all locations) ranging from 18.96% to 26.14% for  $H = 7$  to 28 days ahead forecasting respectively, the only consistent competitor is Crossformer (18.87% to 28.83%). The rest of the methods do not perform well as the task becomes more challenging, reaching average sMAPEs ranging from 35.51% to 45.84% for  $H = 28$  days. Pending a more detailed evaluation (out-of-scope for this work), there is at least partial evidence to support that DEFORMTIME is a SOTA forecaster for ILI [30, 31, 33, 36]. It not only demonstrates a great regression fit, but also captures the overall trend while forecasting 28 days ahead (average correlation is  $> .90$ , see Tables D1, D2, and D3).

We depict the ILI rate forecasts of all models in Appendix G. A snapshot is presented in Figure 2, showcasing 28 days ahead predictions for influenza season 2018/19 in England. We observe that many models resemble the naïve persistence model, providing smooth but shifted and hence uninformative forecasts. DLinear provides the overall worst fit. With the exception of the iTransformer (see Appendix B for a brief justification), competitive baseline models that capture inter-variable dependencies do perform better. However, their estimates are noisy, and either not capable of capturing the onset (TimeMixer) or intensity (Crossformer and less so LightTS) of the influenza season. Contrary to that, DEFORMTIME provides smoother and more accurate forecasts that corroborate our choice to account for both inter- and intra-variable dependencies.

Further experiments, presented in Appendix D.3, provide evidence that DEFORMTIME is also robust to random seed initialisation (Table D4).

### 4.3 Ablation study for DEFORMTIME

We perform an ablation study to understand the contribution of various operations in DEFORMTIME, namely the V-DAB and T-DAB modules, the position embeddings used in DABs (we conventionally denote both by  $\mathbf{P}_{v,t}$ ), and the NAE module with and without position embedding  $\mathbf{P}_n$ . Experiments are conducted on the ILI rate forecasting task for 2 locations, England (ILI-ENG) and US Region 9 (ILI-US9), and across the 4 test seasons. Hyperparameters are re-tuned using the same validation approach separately for each ablation variant.

Table 2 enumerates the ablation outcomes, showing the average MAE across all test periods. Evidently, each component or operation contributes to the reduction of MAE. On average, the V-DAB module provides stronger performance improvements (8.4%) compared to the T-DAB module (4.8%). However, for the longest forecasting horizon ( $H = 28$ ) both modules have a similar level of contribution (respectively, 11.4% and 9.8%). Hence, establishing inter-variable dependencies is always useful, but intra-variable dependencies become more important in longer forecasting horizons.

The inclusion of the NAE component is equally important as it improves MAE by 6.3% on average. Interestingly, the level of relative improvement increases as the forecasting horizon extends (from 5.8% to 7.6%). This potentially highlights that longer forecasting horizons require more abstraction over the feature space, favouring learning from correlated groups of variables. Finally, the use of



Table 2: Ablation study for DEFORMTIME (shortened to DTIME). We report the average MAE over the 4 test periods for tasks ILI-ENG and ILI-US9 across all forecasting horizons ( $H$ ). ‘ $\neg$ ’ denotes the absence of a module or an operation.

	$H$	DTIME	$\neg$ V-DAB	$\neg$ T-DAB	$\neg$ $\mathbf{P}_{v,t}$	$\neg$ NAE	$\neg$ $\mathbf{P}_n$
ILI-ENG	7	<b>1.6417</b>	1.8536	1.8043	1.9420	1.8238	1.8849
	14	<b>2.2308</b>	2.4978	2.3570	2.2646	2.4280	2.8982
	21	<b>2.6500</b>	2.9173	2.6840	2.8838	2.9523	2.9971
	28	<b>2.7228</b>	3.3685	3.2848	3.1082	3.1016	2.8446
	Avg.	<b>2.3113</b>	2.6593	2.5325	2.5497	2.5764	2.6562
	$H$	DTIME	$\neg$ V-DAB	$\neg$ T-DAB	$\neg$ $\mathbf{P}_{v,t}$	$\neg$ NAE	$\neg$ $\mathbf{P}_n$
ILIUS9	7	<b>0.2622</b>	0.2709	0.2649	0.2753	0.2665	0.2737
	14	<b>0.3084</b>	0.3138	0.3103	0.3174	0.3161	0.3270
	21	<b>0.3179</b>	0.3493	0.3236	0.3452	0.3273	0.3355
	28	<b>0.3532</b>	0.3664	0.3623	0.3689	0.3638	0.3693
	Avg.	<b>0.3104</b>	0.3251	0.3153	0.3267	0.3184	0.3264

position embeddings, albeit not entailing a very sophisticated operation, significantly enhances the impact of the V-DAB/T-DAB and NAE modules by 7.2% and 8.9%, respectively. We argue that position embeddings, obtained before ( $\mathbf{P}_n$ ) and after ( $\mathbf{P}_{v,t}$ ) deformation, work in tandem to maintain key information that evidently further improves the overall forecasting accuracy.

#### 4.4 Computational complexity and efficiency of DEFORMTIME

The computational complexity of DEFORMTIME is  $\mathcal{O}(L^2d + Ld^2)$ , where  $L$  denotes the look-back window and  $d$  is the size of the hidden layers throughout the method (see Appendix D.5 for a complete derivation). We note that the number of operations for an encoder layer reduces quadratically as we increase  $r$  (T-DAB’s time window) to values greater than 1. Likewise, segmenting the  $L$  input time steps to patches of a smaller length (in V-DAB) results in quadratic computational benefits.

Overall, DEFORMTIME has a relatively small (GPU VRAM) memory footprint (see Figure D2). Compared to other transformer-based MTS forecasting methods (Crossformer, PatchTST, and iTransformer), our method exhibits consistently low memory consumption as the number of input variables increases (vs. an exponential increase for the other methods). Furthermore, increasing the look-back window does not overly affect memory consumption either (vs. a more accelerated linear increase for Crossformer and PatchTST). Hence, we deduce that DEFORMTIME is adept to MTS forecasting tasks with a considerable amount of exogenous predictors and longer look-back windows.

## 5 Conclusions

We propose DEFORMTIME, a novel deep learning architecture for multivariate time series forecasting that uses deformable attention blocks to effectively learn from exogenous predictors, deploying specific operations that aim to capture inter- and intra-variable dependencies. We assess forecasting accuracy using 3 established benchmark tasks as well as 3 influenza-like illness prediction tasks with web search frequency time series as exogenous variables, covering 3 locations (in 2 countries) and spanning a time period longer than 12 years. DEFORMTIME yields strong forecasting accuracy across the board, reducing mean absolute error on average by 10% compared to the best baseline model (different for each task and horizon) and by at least 15.2% (for Crossformer [55]) when compared to a specific model. Importantly, performance gains remain stable for longer forecasting horizons. Our experiments, including the ablation study, highlight that modelling variable dependencies is an important attribute. Specifically in the disease forecasting task, where more exogenous predictors are present, the most competitive baselines capture variable dependencies to some extent, whereas models that do not on many occasions cannot surpass the performance of a naïve persistence model (see also Appendix D.7). In contrast to other methods, DEFORMTIME’s GPU memory footprint is not significantly affected by the amount of exogenous variables. We discuss the limitations, societal impact, and future directions for this work in Appendices E and F.

## Acknowledgements

V.L. acknowledges all levels of support from the EPSRC grant EP/X031276/1 and a Google donation.

## References

- [1] G. Athanasopoulos, R. J. Hyndman, H. Song, and D. C. Wu. The tourism forecasting competition. *International Journal of Forecasting*, 27(3):822–844, 2011.
- [2] J. L. Ba, J. R. Kiros, and G. E. Hinton. Layer Normalization. *arXiv preprint arXiv:1607.06450*, 2016.
- [3] S. Bontemps, P. Bogaert, N. Titeux, and P. Defourny. An object-based change detection method accounting for temporal dependences in time series with medium to coarse spatial resolution. *Remote Sensing of Environment*, 112(6):3181–3191, 2008.
- [4] Z. Chen, Y. Zhu, C. Zhao, G. Hu, W. Zeng, J. Wang, and M. Tang. DPT: Deformable Patch-based Transformer for Visual Recognition. In *Proceedings of the ACM International Conference on Multimedia*, pages 2899–2907, 2021.
- [5] J. Dai, H. Qi, Y. Xiong, Y. Li, G. Zhang, H. Hu, and Y. Wei. Deformable Convolutional Networks. In *Proceedings of the IEEE International Conference on Computer Vision*, pages 764–773, 2017.
- [6] J. G. De Gooijer and R. J. Hyndman. 25 years of time series forecasting. *International Journal of Forecasting*, 22(3):443–473, 2006.
- [7] C. Deb, F. Zhang, J. Yang, S. E. Lee, and K. W. Shah. A review on time series forecasting techniques for building energy consumption. *Renewable and Sustainable Energy Reviews*, 74:902–924, 2017.
- [8] A. Dosovitskiy, L. Beyer, A. Kolesnikov, D. Weissenborn, X. Zhai, T. Unterthiner, M. Dehghani, M. Minderer, G. Heigold, S. Gelly, J. Uszkoreit, and N. Houlsby. An Image is Worth 16x16 Words: Transformers for Image Recognition at Scale. In *International Conference on Learning Representations*, 2021.
- [9] A. F. Dugas, M. Jalalpour, Y. Gel, S. Levin, F. Torcaso, T. Igusa, and R. E. Rothman. Influenza Forecasting with Google Flu Trends. *PLoS ONE*, 8(2):e56176, 2013.
- [10] J. Ginsberg, M. H. Mohebbi, R. S. Patel, L. Brammer, M. S. Smolinski, and L. Brilliant. Detecting influenza epidemics using search engine query data. *Nature*, 457(7232):1012–1014, 2009.
- [11] L. Han, H. Ye, and D. Zhan. The Capacity and Robustness Trade-off: Revisiting the Channel Independent Strategy for Multivariate Time Series Forecasting. *arXiv preprint arXiv:2304.05206*, 2023.
- [12] G. Huang, Y. Sun, Z. Liu, D. Sedra, and K. Q. Weinberger. Deep Networks with Stochastic Depth. In *Proceedings of the European Conference on Computer Vision*, pages 646–661, 2016.
- [13] Q. Huang, L. Shen, R. Zhang, S. Ding, B. Wang, Z. Zhou, and Y. Wang. CrossGNN: Confronting Noisy Multivariate Time Series Via Cross Interaction Refinement. In *Advances in Neural Information Processing Systems*, 2023.
- [14] R. J. Hyndman and M. S. Ullah. Robust forecasting of mortality and fertility rates: A functional data approach. *Computational Statistics & Data Analysis*, 51(10):4942–4956, 2007.
- [15] J. P. Ioannidis, S. Cripps, and M. A. Tanner. Forecasting for COVID-19 has failed. *International Journal of Forecasting*, 38(2):423–438, 2022.
- [16] Y. Jia, Y. Lin, X. Hao, Y. Lin, S. Guo, and H. Wan. WITRAN: Water-wave information transmission and recurrent acceleration network for long-range time series forecasting. In *Advances in Neural Information Processing Systems*, 2023.
- [17] M. Jin, S. Wang, L. Ma, Z. Chu, J. Y. Zhang, X. Shi, P.-Y. Chen, Y. Liang, Y.-F. Li, S. Pan, and Q. Wen. Time-LLM: Time Series Forecasting by Reprogramming Large Language Models. In *International Conference on Learning Representations*, 2024.
- [18] S. Kandula and J. Shaman. Reappraising the utility of Google Flu Trends. *PLoS Computational Biology*, 15(8):e1007258, 2019.
- [19] G. Lai, W.-C. Chang, Y. Yang, and H. Liu. Modeling Long- and Short-Term Temporal Patterns with Deep Neural Networks. In *Proceedings of the International ACM SIGIR Conference on Research & Development in Information Retrieval*, pages 95–104, 2018.
- [20] V. Lampos, A. C. Miller, S. Crossan, and C. Stefansen. Advances in nowcasting influenza-like illness rates using search query logs. *Scientific Reports*, 5(12760), 2015.

- [21] V. Lampos, B. Zou, and I. J. Cox. Enhancing Feature Selection Using Word Embeddings: The Case of Flu Surveillance. In *Proceedings of the International Conference on World Wide Web*, page 695–704, 2017.
- [22] D. Lazer, R. Kennedy, G. King, and A. Vespignani. The Parable of Google Flu: Traps in Big Data Analysis. *Science*, 343(6176):1203–1205, 2014.
- [23] S. Lee, T. Park, and K. Lee. Learning to Embed Time Series Patches Independently. In *International Conference on Learning Representations*, 2024.
- [24] Y. Li, R. Yu, C. Shahabi, and Y. Liu. Diffusion Convolutional Recurrent Neural Network: Data-Driven Traffic Forecasting. In *International Conference on Learning Representations*, 2018.
- [25] S. Lin, W. Lin, W. Wu, F. Zhao, R. Mo, and H. Zhang. SegRNN: Segment Recurrent Neural Network for Long-Term Time Series Forecasting. *arXiv preprint arXiv:2308.11200*, 2023.
- [26] S. Liu, H. Yu, C. Liao, J. Li, W. Lin, A. X. Liu, and S. Dustdar. Pyraformer: Low-Complexity Pyramidal Attention for Long-Range Time Series Modeling and Forecasting. In *International Conference on Learning Representations*, 2022.
- [27] Y. Liu, H. Wu, J. Wang, and M. Long. Non-stationary Transformers: Exploring the Stationarity in Time Series Forecasting. In *Advances in Neural Information Processing Systems*, 2022.
- [28] Y. Liu, T. Hu, H. Zhang, H. Wu, S. Wang, L. Ma, and M. Long. iTransformer: Inverted Transformers Are Effective for Time Series Forecasting. In *International Conference on Learning Representations*, 2024.
- [29] D. Luo and X. Wang. ModernTCN: A Modern Pure Convolution Structure for General Time Series Analysis. In *International Conference on Learning Representations*, 2024.
- [30] M. Morris, P. Hayes, I. J. Cox, and V. Lampos. Estimating the Uncertainty of Neural Network Forecasts for Influenza Prevalence Using Web Search Activity. *arXiv preprint arXiv:2105.12433*, 2021.
- [31] M. Morris, P. Hayes, I. J. Cox, and V. Lampos. Neural network models for influenza forecasting with associated uncertainty using Web search activity trends. *PLoS Computational Biology*, 19(8):e1011392, 2023.
- [32] Y. Nie, N. H. Nguyen, P. Sinthong, and J. Kalagnanam. A Time Series is Worth 64 Words: Long-term Forecasting with Transformers. In *International Conference on Learning Representations*, 2023.
- [33] D. Osthus and K. R. Moran. Multiscale influenza forecasting. *Nature Communications*, 12(1):2991, 2021.
- [34] H. Pi and C. Peterson. Finding the Embedding Dimension and Variable Dependencies in Time Series. *Neural Computation*, 6(3):509–520, 1994.
- [35] S. S. Rangapuram, M. W. Seeger, J. Gasthaus, L. Stella, Y. Wang, and T. Januschowski. Deep State Space Models for Time Series Forecasting. In *Advances in Neural Information Processing Systems*, 2018.
- [36] N. G. Reich, C. J. McGowan, T. K. Yamana, A. Tushar, E. L. Ray, D. Osthus, S. Kandula, L. C. Brooks, W. Crawford-Crudell, G. C. Gibson, et al. Accuracy of real-time multi-model ensemble forecasts for seasonal influenza in the U.S. *PLoS Computational Biology*, 15(11):e1007486, 2019.
- [37] M. Reichstein, G. Camps-Valls, B. Stevens, M. Jung, J. Denzler, N. Carvalhais, and f. Prabhat. Deep learning and process understanding for data-driven Earth system science. *Nature*, 566(7743):195–204, 2019.
- [38] O. B. Sezer, M. U. Gudelek, and A. M. Ozbayoglu. Financial time series forecasting with deep learning: A systematic literature review: 2005–2019. *Applied Soft Computing*, 90:106181, 2020.
- [39] J. Shaman and A. Karspeck. Forecasting seasonal outbreaks of influenza. *PNAS*, 109(50):20425–20430, 2012.
- [40] P. Shaw, J. Uszkoreit, and A. Vaswani. Self-Attention with Relative Position Representations. In *Proceedings of the Conference of the North American Chapter of the Association for Computational Linguistics: Human Language Technologies, Volume 2 (Short Papers)*, pages 464–468, 2018.
- [41] A. Vaswani, N. Shazeer, N. Parmar, J. Uszkoreit, L. Jones, A. N. Gomez, Ł. Kaiser, and I. Polosukhin. Attention is All you Need. In *Advances in Neural Information Processing Systems*, 2017.
- [42] M. Wagner, V. Lampos, I. J. Cox, and R. Pebody. The added value of online user-generated content in traditional methods for influenza surveillance. *Scientific Reports*, 8(13963), 2018.

- [43] H. Wang, J. Peng, F. Huang, J. Wang, J. Chen, and Y. Xiao. MICN: Multi-scale Local and Global Context Modeling for Long-term Series Forecasting. In *The Eleventh International Conference on Learning Representations*, 2023.
- [44] S. Wang, H. Wu, X. Shi, T. Hu, H. Luo, L. Ma, J. Y. Zhang, and J. Zhou. TimeMixer: Decomposable Multiscale Mixing for Time Series Forecasting. In *International Conference on Learning Representations*, 2024.
- [45] H. Wu, J. Xu, J. Wang, and M. Long. Autoformer: Decomposition Transformers with Auto-Correlation for Long-Term Series Forecasting. In *Advances in Neural Information Processing Systems*, 2021.
- [46] H. Wu, T. Hu, Y. Liu, H. Zhou, J. Wang, and M. Long. TimesNet: Temporal 2D-Variation Modeling for General Time Series Analysis. In *International Conference on Learning Representations*, 2023.
- [47] Z. Wu, S. Pan, G. Long, J. Jiang, X. Chang, and C. Zhang. Connecting the Dots: Multivariate Time Series Forecasting with Graph Neural Networks. In *Proceedings of the ACM SIGKDD International Conference on Knowledge Discovery & Data Mining*, pages 753–763, 2020.
- [48] Z. Xia, X. Pan, S. Song, L. E. Li, and G. Huang. Vision Transformer With Deformable Attention. In *Proceedings of the IEEE/CVF Conference on Computer Vision and Pattern Recognition*, pages 4794–4803, 2022.
- [49] R. Xiong, Y. Yang, D. He, K. Zheng, S. Zheng, H. Zhang, Y. Lan, L. Wang, and T. Liu. On Layer Normalization in the Transformer Architecture. In *Proceedings of the International Conference on Machine Learning*, 2020.
- [50] S. Yang, M. Santillana, and S. C. Kou. Accurate estimation of influenza epidemics using Google search data via ARGO. *PNAS*, 112(47):14473–14478, 2015.
- [51] K. Yi, Q. Zhang, W. Fan, H. He, L. Hu, P. Wang, N. An, L. Cao, and Z. Niu. FourierGNN: Rethinking Multivariate Time Series Forecasting from a Pure Graph Perspective. In *Advances in Neural Information Processing Systems*, 2023.
- [52] K. Yi, Q. Zhang, W. Fan, S. Wang, P. Wang, H. He, N. An, D. Lian, L. Cao, and Z. Niu. Frequency-domain MLPs are More Effective Learners in Time Series Forecasting. In *Advances in Neural Information Processing Systems*, 2023.
- [53] A. Zeng, M. Chen, L. Zhang, and Q. Xu. Are Transformers Effective for Time Series Forecasting? In *Proceedings of the AAAI Conference on Artificial Intelligence*, pages 11121–11128, 2023.
- [54] T. Zhang, Y. Zhang, W. Cao, J. Bian, X. Yi, S. Zheng, and J. Li. Less Is More: Fast Multivariate Time Series Forecasting with Light Sampling-oriented MLP Structures. *arXiv preprint arXiv:2207.01186*, 2022.
- [55] Y. Zhang and J. Yan. Crossformer: Transformer Utilizing Cross-Dimension Dependency for Multivariate Time Series Forecasting. In *International Conference on Learning Representations*, 2023.
- [56] L. Zhao and Y. Shen. Rethinking Channel Dependence for Multivariate Time Series Forecasting: Learning from Leading Indicators. In *International Conference on Learning Representations*, 2024.
- [57] H. Zhou, S. Zhang, J. Peng, S. Zhang, J. Li, H. Xiong, and W. Zhang. Informer: Beyond Efficient Transformer for Long Sequence Time-Series Forecasting. In *Proceedings of the AAAI Conference on Artificial Intelligence*, pages 11106–11115, 2021.
- [58] T. Zhou, Z. Ma, X. Wang, Q. Wen, L. Sun, T. Yao, W. Yin, and R. Jin. FiLM: Frequency improved Legendre Memory Model for Long-term Time Series Forecasting. In *Advances in Neural Information Processing Systems*, 2022.
- [59] T. Zhou, Z. Ma, Q. Wen, X. Wang, L. Sun, and R. Jin. FEDformer: Frequency Enhanced Decomposed Transformer for Long-term Series Forecasting. In *International Conference on Machine Learning*, volume 162, pages 27268–27286, 2022.
- [60] X. Zhu, W. Su, L. Lu, B. Li, X. Wang, and J. Dai. Deformable DETR: Deformable Transformers for End-to-End Object Detection. In *International Conference on Learning Representations*, 2021.

---

## Supplementary Materials

---

### A Data sets for time series forecasting

This section offers a detailed description of the data sets used in our experiments to assess the performance of a series of methods for MTS forecasting. We provide links to data sets that are publicly available. Data sets that were formed by us will be provided in our source code repository. If we cannot share the exact data set due to copyright restrictions, we will provide instructions as to how research teams can obtain access directly from the data provider.

#### A.1 Established MTS forecasting benchmarks

**ETTh1 and ETTh2.** ETTh1 and ETTh2 are electricity transformer temperature data sets that were obtained from 2 different counties in China [57].<sup>8</sup> Each data set contains 6 exogenous variables capturing power load attributes, and the target variable which is the temperature of oil. The data set covers a period from July 1, 2016 to June 26, 2018 (although not all data points are used in our experiments to match the setup in related methods that we compare to). The temporal resolution of these data sets is hourly. Adopting the setup in prior work [28, 32, 46], we use a total amount of 14,400 time steps (starting from July 1, 2016) where the first 8,640 are used for training, the next 2,880 for validation, and the last 2,880 for testing.

**Weather.** The weather data set [45] contains meteorological measurements collected from a weather station at the Max Planck Biogeochemistry Institute. It covers a year from January 1, 2020 to January 1, 2021.<sup>9</sup> The temporal resolution is 10 minutes and 20 meteorological indicators (exogenous variables) are being reported; the target variable is wet-bulb temperature. This results in a total of 52,696 time steps (samples). Based on prior work [55], we use 70%, 10%, and 20% of the time steps for training, validation, and testing, respectively.

#### A.2 Forecasting influenza-like illness rates using web search activity

Important components of our data set are shared in the paper’s online repository.<sup>1</sup> The shared information allows replication of our work for teams who have obtained the same data-sharing agreements (mainly access to the Google Health Trends API). However, we anticipate that we will be permitted to share all data sets (to make replication and comparisons easier).

**Influenza-like illness (ILI) rates.** ILI is defined as the presence of common influenza symptoms (e.g. sore throat, cough, headache, runny nose) in conjunction with high fever. We obtain ILI rates for England (in the United Kingdom) and two US HHS Regions, specifically Region 2 (states of New Jersey and New York) and Region 9 (states of Arizona and California). For England, we obtain ILI rates from the Royal College of General Practitioners (RCGP) that monitors ILI prevalence via an established sentinel network of GP practices throughout the country. An RCGP ILI rate represents the amount of ILI infections in every 100,000 people in the population of England. For the US Regions, data is obtained from the Centers for Disease Control and Prevention (CDC).<sup>10</sup> An ILI rate from CDC represents the proportion of ILI-related doctor consultations over the total amount of consultations (for any health issue). Hence, the units of the ILI rate in these two monitoring systems (RCGP and

---

<sup>8</sup>ETTh1 and ETTh2, [github.com/zhouhaoyi/ETDataset](https://github.com/zhouhaoyi/ETDataset)

<sup>9</sup>The data set can be obtained from Autoformer’s repository, [github.com/thuml/Autoformer](https://github.com/thuml/Autoformer)

<sup>10</sup>US ILI rates (CDC), [gis.cdc.gov/grasp/fluview/fluportaldashboard.html](https://gis.cdc.gov/grasp/fluview/fluportaldashboard.html)



CDC) are different. The time span for the obtained ILI rates is the same as the time span for the web search data (see next paragraphs).

**Influenza season definition.** An annual influenza season for the HHS US Regions is assumed to start on August 1 of year  $\chi$  and end on July 31 of year  $\chi+1$ . For England, this is shifted by a month, i.e. an annual influenza season starts on September 1 of year  $\chi$  and ends on August 31 of year  $\chi+1$ .

**Linear interpolation of weekly ILI rates.** ILI rates are reported on a weekly basis. To generate daily data (that increases the amount of training samples by a factor of 7), we use linear interpolation. It should be noted that for RCGP, Monday determines the start of a week, while for CDC this is determined by Sunday (different ISO specification). We assume that the weekly reported ILI rate is representative of the middle day of a week (Thursday for England and Wednesday for the US Regions) and the ILI rates are then linearly interpolated accordingly.

**Real-time delay in ILI rate availability.** We also note that in practice, the reported ILI rate is delayed, i.e. assuming that it is published by RCGP or CDC at time  $t$ , it actually refers to an ILI rate representing a previous time  $t-\delta$ . Specifically, we consider that there is a delay of  $\delta=7$  days for RCGP/England, and a delay of  $\delta=14$  days for CDC/US Regions [36, 42]. This delay,  $\delta$ , has an impact on the autoregressive time series (of the target variable, in this case, the ILI rate) in a forecasting task (see also section 2). As the delay increases, the forecaster is expected to rely more on the exogenous predictors (that are not delayed) rather than the autoregressive time series of the target variable.

**Web search frequency time series.** Web search activity trends, if modelled appropriately [10, 18, 20, 22], are a good indicator of influenza rates in a population and can become a strong exogenous predictor for influenza forecasting [9, 31]. We obtain web search activity data from the Google Health Trends API; this is not a publicly available API, but access can be provided via an application process.<sup>11</sup> For a day and a certain location, the frequency of a search query is determined as the ratio of searches conducted for a particular term or set of terms divided by the overall search volume. We use a pool of 22,071 unique health-related search queries and obtain their daily frequency from August 1 (US regions) or September 1 (England), 2006 to July 31 (US regions) or August 31 (England), 2019. However, we note that not all search queries are used as exogenous variables in our forecasting models. A feature selection process is described in Appendix A.3.

Given that for the US, we can only obtain data at the state level (as opposed to regional), we use a weighted average of the state-level search query frequencies. The weights are based on the population of each state. In particular, for Region 2, the states of New Jersey and New York have weights of 0.32 and 0.68, whereas for Region 9, the states of Arizona and California have weights of 0.16 and 0.84, respectively. Note that smaller locations (or distant ones) that may be part of an HHS Region are excluded from the web search data sets; given their relatively small population, these locations do not have a significant impact on the reported ILI rates and the data obtained from the Google Health Trends API are quite sparse.

**Training, validation, and test sets.** We assess the accuracy of forecasters across the last 4 influenza seasons (4 separate test sets) in England and the US regions. Each test period is a complete influenza season (as previously defined). For each test period, we train models based on the 9 influenza seasons that precede it. A part of each training set is used for validating model decisions, including hyperparameters. We construct validation sets using the following strategy. Each validation set has 180 days in total, using 60-day periods to capture the onset, peak, and the period after the peak (or the outset) of an influenza season. Each 60-day period comes from a different influenza season in the training set; we use the last 3 influenza seasons in the training data to make sure our validation process has a recency effect. The last, penultimate, and third from last influenza seasons are used to define the outset, peak, and onset validation periods, respectively. We use CDC's definition to determine the onset of an influenza season, i.e. a time point is deemed to be the onset when the subsequent ILI rates exceed a threshold for 2 consecutive weeks.<sup>12</sup> The peak point is simply the highest ILI rate within an influenza season. The outset has the inverse definition from the onset, i.e.

<sup>11</sup>Google Health Trends API access application, [support.google.com/trends/contact/trends\\_api](https://support.google.com/trends/contact/trends_api)

<sup>12</sup>CDC's influenza season onset definition, [cdc.gov/flu/weekly/overview.htm](https://cdc.gov/flu/weekly/overview.htm)

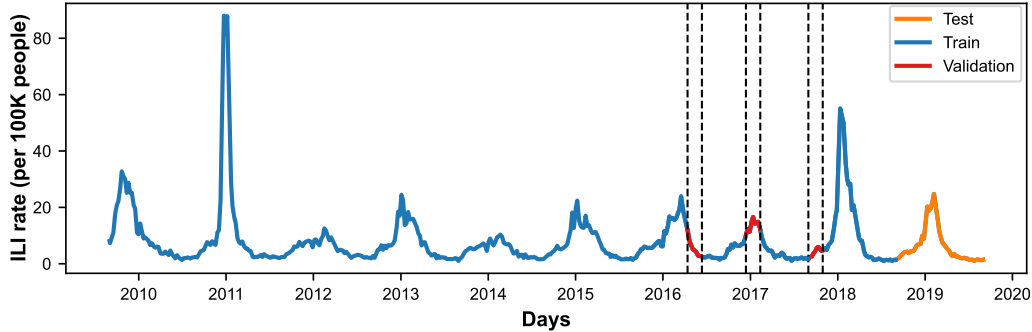


Figure A1: An example of how the training, validation, and test sets are constructed when the test influenza season is 2018/19 (England). The lines in blue, red, and orange colour denote the training, validation, and test periods, respectively. To form the validation set from our training data, we select the period after the peak (outset) from the third to last influenza season, the period around the peak from the penultimate season, and a period around influenza onset from the last season.

the last time point where the ILI rate exceeds the onset threshold for two consecutive weeks. Once these time points are determined, they become the 30th point in a 60-day validation period. Figure A1 shows an example of the validation periods that were determined when training an ILI rate model for England using (training) data from September 2009 to August 2018 (with the test period being September 2018 to August 2019).

### A.3 Feature selection for web search activity time series

Originally, we consider 22,071 search queries. We then perform two feature selection steps to maintain more relevant queries to the ILI forecasting task. First, we apply a semantic filter to remove queries that are not related to the topic of influenza, similarly to the approach presented by Lamos et al. [21]. We obtain an embedding representation for each search query using a pre-trained sentence BERT model.<sup>13</sup> We also obtain the embeddings of influenza-related (base) terms and expressions, such as “flu”, “flu symptoms” etc. We compute the cosine similarity between each base term and search query and maintain the top-1000 (England) or top-500 (US regions) search queries (per base term). This leaves 4,396 and 2,479 queries respectively for England and the US regions.<sup>14</sup> The second selection step is dynamic, i.e. it might have a different outcome as the training data change. In this step, we compute the linear correlation between the remaining search queries and the target variable (ILI rate) in the 5 most recent influenza seasons in the training data (to impose recency). We maintain search queries with a correlation that exceeds a correlation threshold  $\tau$ , which is a learnable hyperparameter (see also Appendix C).

### A.4 Data normalisation

In all forecasting tasks, we standardise all variables, an operation also known as z-scoring (zero mean, unit standard deviation), each time based on the training data. The prediction output is de-normalised back to its original scale prior to being compared with the (de-normalised) ground truth. In addition to that, for the ETT and weather data sets, we also z-score each variable within the input’s look-back window, in accordance with previous work [27, 32, 58].

### A.5 Criticism of data sets used to benchmark forecasting methods

Although we present results using the ETTh1, ETTh2, and weather data sets to compare with other forecasting methods in the literature, we consider these data sets to have several shortcomings. Clearly, a weather data set that covers only a 1-year period and is based on the sensors from just one geographical location cannot be expected to provide good enough insights into meteorological

<sup>13</sup>Sentence BERT, [huggingface.co/bert-base-uncased](https://huggingface.co/bert-base-uncased)

<sup>14</sup>Base and filtered search terms are provided in DEFORMTIME’s repository (see footnote 1).

forecasting. It captures a negligible portion of meteorological data and, as a result, derived forecasting models cannot have any practical impact (compared to actual models that are used in meteorology). Hence, using this data set for training and evaluating a forecasting model may, unfortunately, result in misleading or at least inconclusive outcomes. Similar issues, but perhaps to a smaller extent, are present in the ETTh1 and ETTh2 data sets. On the one hand, these data sets seem to have a more solid practical application. However, experiments on their ETTm1 and ETTm2 variants, where the temporal resolution changes from 1 hour to 15 minutes (same data, shorter temporal resolution), showcase part of the problem. When we compared the forecasting performance of SOTA baselines between the two different temporal resolutions, we surprisingly found that the prediction based on the hourly sampled data set has better accuracy compared to the quarter-hourly sampled data set even at longer forecasting horizons. For example, models that conduct 192 or even 336 time steps (equivalent to 8 or 14 days) ahead forecasting with ETTh1 and ETTh2 achieve a lower MAE compared to a 720 time steps ahead forecast with ETTm1 and ETTm2 (equivalent to 7.5 days ahead forecast), respectively [29, 32, 46].

We also noticed that some papers run experiments on US national weekly ILI rates obtained from the CDC [32, 43, 59]. The first concerning observation was that in these experiments, the input variables were based on variates (columns) from the CDC extract (spreadsheet) that only provide redundant insights compared to the ILI rate (e.g. the raw numerator and denominator of an ILI rate or the population unweighted ILI rate). In addition, some forecasting horizons that were explored in these benchmarks were practically unreasonable (even from a biological perspective, there are limits in predicting the future, especially when it comes to viruses). SOTA forecasting models for influenza generally provide good accuracy at approximately a 2 weeks ahead forecasting horizon [31, 33]. Anything beyond that with satisfactory performance should be considered as a very important development within the disease modelling community. We do think DEFORMTIME might fall in that category as it delivers good results for 3 or 4 weeks ahead forecasting horizons. Contrary to that, in the aforementioned ILI rate benchmark, there were forecasting horizons of 24 or 60 weeks ahead (i.e. even more than a year!). Of course, the accuracy of the forecasting models under these forecasting horizons was reportedly detrimentally poor (influenza does not have a strong periodicity), and consequently could not be used for any meaningful comparative conclusions. If all forecasting models are performing poorly, even the least poorly performing one still is an inadequate forecaster (for the underlying task).

Beyond this, we have also excluded data sets, such as traffic [45] and electricity consumption [57], that do not have one explicitly defined target variable, but instead focus on multivariate predictions (multi-task learning). Consequently, these data sets are not entirely compatible with our forecasting task or method (DEFORMTIME makes predictions about one target variable).

To compensate for that we have developed a set of 3 influenza forecasting tasks. Models from these tasks can find direct real-world applications, i.e. become part of influenza monitoring systems in England or the US. The evaluation process is rigorous, i.e. across 4 consecutive influenza seasons as opposed to using 1 fixed test period that may again lead to biased insights.

## B Summary of other forecasting models

Here we provide a list of the models that we are comparing DEFORMTIME to:

- **LightTS** [54] uses MLP layers as the building blocks to extract both inter-variable and intra-variable dependencies upon time series with different temporal resolutions.
- **DLinear** [53] uses a fully connected layer along the temporal dimension with seasonal-trend decomposition to regress the historical values for future predictions.
- **Crossformer** [55] is a transformer-based model that divides the input into patches and proposes a two-stage attention layer to capture inter- and intra-variable dependencies.
- **PatchTST** [32] is a transformer-based model that takes segmented patches as input tokens for the model. The prediction of each variable is designed to be independent of one another, i.e. with no inter-variable dependencies established.
- **iTransformer** [28] is a transformer-based model that embeds the sequence dimension rather than the input variable dimension. It currently provides the SOTA performance on the long-term forecast

tasks.<sup>15</sup> We note that although iTransformer captures inter-variable dependencies, it achieves that by embedding the input along the sequence dimension. This disrupts the temporal structure within each variable, leading to a sub-optimal performance in our empirical evaluation.

- **TimeMixer** [44] is an MLP-based model that predicts the seasonal and trend components at different sampling scales and mixes forecasts to form the final prediction. Note that the authors consider variable mixing optional for their model. We opted to deploy the version that conducts variable mixing for the ILI rate forecasting tasks.
- The **persistence model** is a naïve baseline that uses the last seen value of the target variable in the input as the forecast.

## C Supplementary experiment settings

This section is supplementary to section 4.1 in the main paper. All experiments were conducted (in parallel) using a server with 2 NVIDIA A40 GPUs.

### C.1 Input variable re-arrangement based on correlation with the target variable

In the ETT and weather forecasting tasks, we rearrange variables (see NAE in section 3.2) based on their linear correlation with the target variable across all time steps preceding the validation set. In the ILI rate forecasting tasks where training sets cover a period of 9 years prior to the test period, we only use the last 5 influenza seasons in the training set to obtain correlations. This is because both user search behaviour and search engine characteristics (e.g. automatic search suggestions) evolve, and this approach to feature selection reinforces a weak recency effect that is ultimately beneficial to prediction accuracy [31, 50].

### C.2 DEFORMTIME setup

We use  $G = 4$  variable neighbourhoods throughout (see section 3.2). This setting ( $G = 4$ ) also determines the number of group partitions for offset generation and multi-head attention in T-DAB (section 3.4). The learnable amplitude  $\alpha \in \{3, 5, 7, 9\}$  (see sections 3.3 and 3.4) is tuned collectively for both V-DAB and T-DAB. We keep the kernel size  $k$  of the interpolation functions  $\phi(\cdot)$  and  $\psi(\cdot)$  identical to  $\alpha$  throughout the experiments. In all experiments, DEFORMTIME has 2 encoder layers (see section 3.5). For the ETT and weather tasks, we set  $r = 1$  in the first encoder layer and select from  $r \in \{6, 12, 24\}$  time steps in the second encoder layer (see section 3.4). In addition, we select the segmentation length from  $\ell \in \{6, 12, 24\}$  time steps (see section 3.3) collectively for both encoder layers. Given the more direct weekly temporal resolution in the reported ILI rates and the fact that web search activity trends do have weekly patterns, in the ILI forecasting task, we set  $\ell = 7$  time steps (days), and also set  $r = 1$  and  $r = 7$  time steps in the first and second encoder layer, respectively. The segmentation stride  $s$  is kept the same as  $\ell$  throughout the experiments.

### C.3 Optimisation and hyperparameter settings

The look-back window  $L$  is set to 336 time steps for the ETTh1, ETTh2, and weather forecasting tasks, based on Nie et al. [32]. For influenza forecasting, we set  $L$  to  $\{28, 28, 56, 56\}$  days for forecasting horizons  $H = \{7, 14, 21, 28\}$  days ahead, respectively. Only for influenza forecasting, we also set the batch size and  $d$  to 64. For the other tasks, these become learnable parameters (see next section). The number of training epochs is set to 100 for ETTh1, ETTh2, and weather tasks and 50 for the influenza forecasting task. Neural networks are optimised with Adam using mean squared error loss on all outputs. Note that the output can be a time series (sequence) of one variable (the target) or more variables (target and exogenous) depending on the forecasting method. As an exception, we use MAE loss for all models tuned on the weather forecasting task. Training stops early when the validation error of the target variable at time  $t + H$  does not decrease further (compared to its lowest value) for 5 consecutive epochs. We then use the model with the lowest validation loss.

For the ILI rate forecasting tasks, all models are trained with a fixed random seed equal to ‘42’. For ETTh1, ETTh2, and weather tasks, we fix the seed to ‘2021’ based on previous work [32, 44, 53],

<sup>15</sup>Long-term forecast tasks ranking, [github.com/thuml/Time-Series-Library](https://github.com/thuml/Time-Series-Library)

Table D1: ILI rate forecasting accuracy results in England (ILI-ENG) using web search frequency time series as exogenous variables.  $\rho$  and  $\epsilon$  % denote linear correlation and sMAPE, respectively. The best results are in **bold** font and the second best are underlined.

$H$	Model	2015/16			2016/17			2017/18			2018/19			Average		
		$\rho$	MAE	$\epsilon$ %	$\rho$	MAE	$\epsilon$ %	$\rho$	MAE	$\epsilon$ %	$\rho$	MAE	$\epsilon$ %	$\rho$	MAE	$\epsilon$ %
7	Persistence	0.9072	<u>1.7077</u>	22.43	0.9129	<u>1.2287</u>	22.67	0.8539	4.0441	31.08	0.8944	1.7037	23.67	0.8921	2.1710	<b>24.96</b>
	DLinear	0.8710	2.6985	38.86	0.8769	1.6879	33.77	0.8231	4.2734	50.14	0.8906	2.6258	49.30	0.8654	2.8214	43.02
	PatchTST	0.8832	1.9823	26.13	0.8744	1.4307	25.39	0.8475	3.7925	31.23	0.8526	2.0403	27.70	0.8644	2.3115	27.61
	iTransformer	0.8773	2.0645	27.26	0.8911	1.3734	24.06	0.8180	4.1077	31.26	0.8911	1.6881	<u>22.94</u>	0.8694	2.3084	26.38
	TimeMixer	0.9056	1.7179	<u>22.27</u>	0.8616	1.4676	24.97	0.8694	3.4828	28.09	0.8388	2.0310	27.39	0.8688	2.1748	<u>25.68</u>
	LightTS	0.8385	2.2625	38.87	0.9432	2.4880	89.24	<u>0.9441</u>	<u>2.6512</u>	52.01	0.9426	1.5570	28.87	0.9171	2.2397	52.25
	Crossformer	0.8879	2.3314	36.08	<u>0.9591</u>	<b>0.8606</b>	<b>17.82</b>	0.9234	2.9133	<b>27.04</b>	<u>0.9436</u>	<u>1.3737</u>	<b>21.89</b>	<u>0.9285</u>	<u>1.8698</u>	25.71
	DEFORMTIME	<b>0.9728</b>	<b>1.3786</b>	<b>19.57</b>	<b>0.9665</b>	1.3083	29.49	<b>0.9585</b>	<b>2.6313</b>	41.40	<b>0.9436</b>	<b>1.2485</b>	23.96	<b>0.9603</b>	<b>1.6417</b>	28.61
	14	Persistence	0.8292	2.3161	<u>30.16</u>	0.8414	1.6867	29.54	0.7289	5.8180	42.30	0.8031	2.4291	33.08	0.8006	3.0625
DLinear		0.7810	3.6354	52.29	0.7857	2.1872	42.47	0.6834	5.5368	60.91	0.8351	3.8092	65.47	0.7713	3.7922	55.28
PatchTST		0.8078	2.6267	35.59	0.7730	1.9562	33.55	0.6722	5.6075	43.64	0.7218	2.8284	38.25	0.7437	3.2547	37.76
iTransformer		0.7731	2.7620	36.46	0.7776	1.9929	34.17	0.6576	5.7796	44.34	0.7850	2.3862	31.71	0.7483	3.2301	36.67
TimeMixer		0.7706	2.6783	34.25	0.8684	1.5621	<u>29.06</u>	0.7164	5.0940	39.59	0.7503	2.7491	38.66	0.7764	3.0209	35.39
LightTS		0.8109	2.5494	32.28	<u>0.9233</u>	1.6292	36.46	0.7821	4.4367	<u>39.46</u>	0.8915	<u>2.1365</u>	44.97	0.8519	2.6879	38.29
Crossformer		0.7940	2.9124	41.75	0.8843	<u>1.4711</u>	<b>23.39</b>	0.8470	<u>3.8295</u>	<b>30.88</b>	<u>0.9007</u>	2.4044	<b>27.86</b>	<u>0.8565</u>	<u>2.6543</u>	<b>30.97</b>
DEFORMTIME		<b>0.9259</b>	<b>2.0556</b>	<b>25.36</b>	<b>0.9400</b>	<b>1.3180</b>	33.86	<b>0.8964</b>	<b>3.7631</b>	47.33	<b>0.9154</b>	<b>1.7863</b>	<u>29.36</u>	<b>0.9194</b>	<b>2.2308</b>	33.98
21		Persistence	0.7357	2.8604	36.98	0.7465	2.1552	36.45	0.6002	7.3119	52.46	0.6952	3.1193	42.23	0.6944	3.8617
	DLinear	0.4466	4.1958	56.02	0.6441	2.8294	52.56	0.4920	6.9514	71.66	0.6608	3.9192	64.75	0.5609	4.4739	61.25
	PatchTST	0.6126	3.6607	48.57	0.6214	2.6377	44.77	0.4427	7.3828	60.54	0.5861	3.5956	50.55	0.5657	4.3192	51.11
	iTransformer	0.5310	4.1390	55.62	0.5987	2.6718	43.65	0.4403	7.0816	55.17	0.6556	3.0464	<u>41.29</u>	0.5564	4.2347	48.93
	TimeMixer	0.5398	3.8805	56.71	0.7799	<b>1.7940</b>	<b>30.45</b>	0.7497	5.5338	58.68	0.7539	2.9919	51.58	0.7058	3.5501	49.36
	LightTS	0.7082	3.3630	45.16	<u>0.8696</u>	1.9335	58.65	0.8132	5.6422	51.74	<u>0.8594</u>	<u>2.5078</u>	51.59	<u>0.8126</u>	3.3616	51.78
	Crossformer	0.8113	<u>2.6710</u>	<u>36.42</u>	0.8014	<u>1.8035</u>	31.29	<u>0.8504</u>	<b>4.5615</b>	49.08	0.7331	2.9697	45.48	0.7991	3.0014	<u>40.57</u>
	DEFORMTIME	<b>0.8819</b>	<b>2.1700</b>	<b>27.01</b>	<b>0.8859</b>	1.8980	32.65	<b>0.9110</b>	<u>4.8984</u>	<b>44.78</b>	<b>0.9092</b>	<b>1.6335</b>	<b>26.36</b>	<b>0.8970</b>	<b>2.6500</b>	<b>32.70</b>
	28	Persistence	0.6408	3.3786	43.17	0.6344	2.6018	42.68	0.4813	8.5576	60.33	0.5733	3.8047	51.79	0.5825	4.5857
DLinear		0.3917	4.5039	60.30	0.5078	3.3928	60.94	0.3911	7.7738	77.58	0.5774	4.4683	72.19	0.4670	5.0347	67.75
PatchTST		0.4271	4.5240	60.22	0.4477	3.2658	53.01	0.3203	8.0693	65.91	0.4486	4.1265	59.27	0.4109	4.9964	59.60
iTransformer		0.3492	4.9542	65.45	0.6761	2.2745	38.38	0.2947	8.3463	69.39	0.5286	3.6750	<u>48.18</u>	0.4622	4.8125	55.35
TimeMixer		0.5395	3.8587	57.17	0.6890	2.4063	45.76	0.4882	6.7783	62.93	0.6632	3.4318	52.52	0.5950	4.1188	54.60
LightTS		0.5812	3.4254	43.91	<u>0.8311</u>	1.9020	<u>36.26</u>	0.7151	6.0675	83.54	0.8900	<u>2.2578</u>	58.66	0.7543	3.4132	55.59
Crossformer		0.7299	<u>3.1253</u>	<b>41.56</b>	0.8082	<u>1.8197</u>	<b>33.57</b>	<u>0.7841</u>	<u>5.4882</u>	<u>55.97</u>	0.9349	2.3599	53.48	<u>0.8143</u>	<u>3.1983</u>	<u>46.14</u>
DeformTime		<b>0.7919</b>	<b>2.6540</b>	49.29	<b>0.9229</b>	<b>1.8100</b>	41.87	<b>0.8493</b>	<b>4.8324</b>	<b>37.53</b>	<b>0.9499</b>	<b>1.5947</b>	<b>33.06</b>	<b>0.8785</b>	<b>2.7228</b>	<b>40.44</b>

with the exception of iTransformer where we set the seed to ‘2023’ in accordance with the official configuration.

#### C.4 Hyperparameter validation

Learnable hyperparameters are determined using grid search. For the ETT and weather forecasting tasks, the batch size and the hidden dimension  $d$  are both selected from  $\{16, 32, 64\}$ . For all tasks, Adam’s initial learning rate is selected from  $\{2, 1, .5, .2, .1, .05\} \times 10^{-3}$  and decayed to 0 with a linear decay scheduler applied after every epoch. Depending on the model, the dropout (most baselines) or the layer drop rate (DEFORMTIME) is selected from  $\{0, .1, .2\}$ .

In the ILI rate forecasting task, the number of exogenous variables we use is a learnable parameter that depends on the linear correlation threshold  $\tau$  (see Appendix A.3). For US regions,  $\tau$  is selected from  $\{.3, .4, .5\}$ . For England,  $\tau$  is selected from  $\{.05, .1, .2, .3, .4, .5\}$ . Given these thresholds, a model can select from 13 to 51 search queries for US regions and from 80 to 752 for England (the higher the correlation threshold, the fewer queries are being selected). Note that for Crossformer, we restricted  $\tau \in \{.3, .4, .5\}$  for all locations as the model required an excessive amount of GPU memory for larger sets of exogenous variables (see also section 4.4 and Appendix D.5).

## D Supplementary results

### D.1 Symmetric Mean Absolute Percentage of Error

To compare results across different tasks that have different units, we use the sMAPE metric. We note the general (and correct) perception that occasionally sMAPE may mislead (by over- or under-estimating error), and hence it can only be used for partial insights in conjunction with a more robust error metric. Hence, our main error metric is MAE. For the ILI rate forecasting tasks, we additionally show linear correlation as an established metric in related literature [10, 20, 50].



Table D2: ILI rate forecasting accuracy results in US Region 2 (ILI-US2) using web search frequency time series as exogenous variables.  $\rho$  and  $\epsilon$  % denote linear correlation and sMAPE, respectively. The best results are in **bold** font and the second best are underlined.

H	Model	2015/16			2016/17			2017/18			2018/19			Average		
		$\rho$	MAE	$\epsilon$ %	$\rho$	MAE	$\epsilon$ %	$\rho$	MAE	$\epsilon$ %	$\rho$	MAE	$\epsilon$ %	$\rho$	MAE	$\epsilon$ %
7	Persistence	0.7758	0.4114	22.26	0.8271	0.6803	24.57	0.7589	1.0284	25.48	0.8954	0.4696	17.59	0.8143	0.6474	22.48
	DLinear	0.7456	0.4982	29.23	0.7980	0.8210	31.85	0.7133	1.0910	30.82	0.8955	0.5318	19.84	0.7881	0.7355	27.94
	PatchTST	0.7666	0.4290	23.78	0.7973	0.7546	26.97	0.6937	1.1018	26.52	0.8624	0.5533	20.79	0.7800	0.7097	24.52
	iTransformer	0.7986	0.3865	<b>21.30</b>	0.8171	0.7367	27.07	0.7784	0.9080	23.22	0.8545	0.5717	21.38	0.8122	0.6507	23.24
	TimeMixer	0.8237	0.3842	21.76	0.8710	0.6449	24.16	<u>0.9124</u>	0.6255	17.87	0.8877	0.4588	16.49	0.8737	0.5284	20.07
	LightTS	0.7930	0.4045	23.23	0.9056	0.5806	<b>18.01</b>	<b>0.9359</b>	<u>0.5688</u>	<u>15.39</u>	0.9451	0.2989	<b>10.33</b>	0.8949	0.4632	16.74
	Crossformer	<u>0.8796</u>	<b>0.3382</b>	<u>21.39</u>	<u>0.9107</u>	<u>0.4975</u>	<u>18.32</u>	0.9009	0.6309	15.61	<u>0.9523</u>	<u>0.2936</u>	<u>10.52</u>	<u>0.9109</u>	<u>0.4400</u>	<u>16.46</u>
	DEFORMTIME	<b>0.8887</b>	<u>0.3428</u>	21.86	<b>0.9463</b>	<b>0.4796</b>	18.66	0.9008	<b>0.5369</b>	<b>12.88</b>	<b>0.9622</b>	<b>0.2894</b>	10.64	<b>0.9245</b>	<b>0.4122</b>	<b>16.01</b>
14	Persistence	0.6872	0.5000	26.67	0.7617	0.8545	31.23	0.6331	1.3027	32.42	0.8436	0.5966	22.65	0.7314	0.8135	28.24
	DLinear	0.6546	0.5761	33.62	0.7335	0.9406	36.90	0.6007	1.2213	34.62	0.8261	0.6360	23.74	0.7037	0.8435	32.22
	PatchTST	0.6628	0.5103	27.27	0.7350	0.9267	34.44	0.5993	1.3085	31.82	0.7922	0.7085	26.90	0.6973	0.8635	30.11
	iTransformer	0.6864	0.4894	26.35	0.7548	0.8934	33.26	0.6025	1.1639	30.28	0.8294	0.6115	22.78	0.7183	0.7896	28.17
	TimeMixer	0.7741	0.4438	25.01	0.8403	0.7314	27.32	0.8043	0.8911	25.13	0.8622	0.5560	20.99	0.8202	0.6556	24.61
	LightTS	0.7203	0.5086	28.62	0.8601	0.7079	<u>22.95</u>	<b>0.9191</b>	<u>0.6698</u>	23.47	<u>0.9409</u>	0.4445	17.40	<u>0.8601</u>	<u>0.5827</u>	23.11
	Crossformer	<u>0.7872</u>	<b>0.4357</b>	<u>24.61</u>	<u>0.8640</u>	<u>0.6502</u>	22.95	0.8057	0.8159	<u>20.83</u>	0.9241	<u>0.4389</u>	<u>15.54</u>	0.8453	0.5852	<u>20.98</u>
	DEFORMTIME	<b>0.8050</b>	<u>0.4404</u>	<b>23.82</b>	<b>0.9271</b>	<b>0.5029</b>	<b>18.53</b>	<u>0.9126</u>	<b>0.6351</b>	<b>16.34</b>	<b>0.9652</b>	<b>0.3226</b>	<b>12.21</b>	<b>0.9025</b>	<b>0.4752</b>	<b>17.73</b>
21	Persistence	0.5918	0.5680	30.04	0.7017	1.0055	37.20	0.5137	1.5443	38.93	0.7792	0.7361	27.88	0.6466	0.9635	33.51
	DLinear	0.6016	0.6023	35.11	0.6897	0.9671	38.06	0.4966	1.3272	38.76	0.7936	0.7530	27.80	0.6454	0.9124	34.93
	PatchTST	0.5775	0.5592	29.41	0.6286	1.1661	43.41	0.5189	1.4395	38.13	0.6478	0.9495	35.86	0.5932	1.0286	36.70
	iTransformer	0.6418	0.4790	<b>24.54</b>	0.7515	0.8784	34.22	0.8230	1.0845	31.85	0.7321	0.7748	29.52	0.7371	0.8042	30.03
	TimeMixer	0.7368	0.4655	27.79	0.8281	0.7853	31.00	0.8509	0.9275	30.07	0.8803	0.5394	21.86	0.8240	0.6794	27.68
	LightTS	<b>0.8484</b>	0.5606	32.47	0.8936	0.6749	34.80	<u>0.9177</u>	<u>0.8065</u>	28.47	0.8951	0.6310	21.34	<b>0.8887</b>	0.6683	29.27
	Crossformer	0.7729	0.4634	26.54	0.8996	0.6688	<b>25.62</b>	0.7621	0.8882	<u>23.17</u>	0.9354	0.4777	<b>13.82</b>	0.8425	0.6245	<u>22.29</u>
	DEFORMTIME	0.7414	<b>0.4568</b>	<u>25.94</u>	<b>0.9028</b>	<b>0.6189</b>	<u>26.44</u>	<b>0.9313</b>	<b>0.6981</b>	<b>21.04</b>	<b>0.9408</b>	<b>0.3963</b>	<u>15.09</u>	<u>0.8791</u>	<b>0.5425</b>	<b>22.13</b>
28	Persistence	0.4860	0.6393	33.84	0.6374	1.1447	42.55	0.4046	1.7516	44.79	0.7071	0.8674	32.98	0.5588	1.1007	38.54
	DLinear	0.4836	0.6512	37.96	0.6112	1.0328	41.19	0.4125	1.4045	40.27	0.6840	0.8337	31.08	0.5479	0.9805	37.62
	PatchTST	0.4013	0.6678	36.55	0.5274	1.2615	48.85	0.3903	1.6234	44.67	0.5579	1.0576	40.39	0.4692	1.1525	42.61
	iTransformer	0.5258	0.5949	32.54	0.6567	1.0632	41.38	0.5726	1.3053	38.82	0.6738	0.8842	34.26	0.6072	0.9619	36.75
	TimeMixer	0.5756	0.5835	36.06	0.7251	1.0106	39.21	0.7694	1.2470	43.49	0.7467	0.7000	27.37	0.7042	0.8853	36.53
	LightTS	<u>0.8262</u>	0.6018	33.56	0.8332	0.8180	31.54	<b>0.8556</b>	0.8913	27.03	<u>0.9011</u>	0.5589	18.78	<b>0.8540</b>	0.7175	27.73
	Crossformer	0.7102	<b>0.4697</b>	<u>27.38</u>	<u>0.9064</u>	<u>0.7624</u>	<u>28.93</u>	0.8432	<u>0.8253</u>	<u>20.69</u>	0.8782	0.5474	<u>18.64</u>	0.8345	<u>0.6512</u>	<u>23.91</u>
	DeformTime	<b>0.8369</b>	<u>0.4716</u>	<b>27.21</b>	<b>0.9562</b>	<b>0.6017</b>	<b>25.66</b>	<b>0.9253</b>	<b>0.5954</b>	<b>17.62</b>	<b>0.9294</b>	<b>0.5463</b>	<b>18.52</b>	<b>0.9119</b>	<b>0.5538</b>	<b>22.25</b>

We use the following definition of sMAPE. For a series of estimates  $\hat{y} \in \mathbb{R}^n$  and a corresponding series of true values  $y \in \mathbb{R}^n$ , sMAPE is given by

$$\text{sMAPE}(\hat{y}, y) = \frac{100}{n} \sum_{j=1}^n \frac{|\hat{y}_j - y_j|}{0.5(|\hat{y}_j| + |y_j|)}. \quad (12)$$

In Tables throughout the manuscript, we denote sMAPE by using  $\epsilon$  %.

## D.2 Detailed ILI forecasting results

Complete results (all test periods, models, and forecasting horizons) in the ILI rate forecasting tasks for England (ILI-ENG), US Region 2 (ILI-US2), and US Region 9 (ILI-US9) are presented in Tables D1, D2, and D3, respectively. In addition to MAE and sMAPE, we also show the linear correlation (denoted by  $\rho$ ) between estimates and the target variable throughout each test period.

## D.3 Seed robustness for DEFORMTIME

We have examined the robustness of DEFORMTIME across different seeds with hyperparameter tuning by re-running the experiments on the ILI-ENG data set across all forecasting horizons and test sets. The results are enumerated in Table D4. The seed used for the results presented in the main paper ('42') provided a performance that did not deviate significantly compared to other seeds. Hence, we conclude that DEFORMTIME is robust to random seed initialisation. We note that compared to the average performance across the explored seeds, seed '42' provides a rather conservative estimate.

## D.4 Ablation study for DEFORMTIME – Additional information

Here we provide additional details to supplement the ablation study presented in section 4.3.

– V-DAB: Denotes that we train a DEFORMTIME model without the V-DAB encoder branch (see section 3.3). Within each encoder layer, we only use the T-DAB branch for sequence encoding.

Table D3: ILI rate forecasting accuracy results in US Region 9 (ILI-US9) using web search frequency time series as exogenous variables.  $\rho$  and  $\epsilon$  % denote linear correlation and sMAPE, respectively. The best results are in **bold** font and the second best are underlined.

H	Model	2015/16			2016/17			2017/18			2018/19			Average		
		$\rho$	MAE	$\epsilon$ %	$\rho$	MAE	$\epsilon$ %	$\rho$	MAE	$\epsilon$ %	$\rho$	MAE	$\epsilon$ %	$\rho$	MAE	$\epsilon$ %
7	Persistence	0.8384	0.3945	18.58	0.8494	0.2791	16.25	0.7304	0.5949	21.55	0.8898	0.3543	17.57	0.8270	0.4057	18.49
	DLinear	0.8071	0.4769	25.07	0.8092	0.3727	22.02	0.6759	0.5704	22.96	0.8925	0.4499	23.82	0.7962	0.4675	23.47
	PatchTST	0.8248	0.3993	19.30	0.8318	0.2802	16.91	0.7068	0.6078	23.25	0.8796	0.3592	17.91	0.8107	0.4116	19.34
	iTransformer	0.8380	0.3736	17.55	0.8446	<u>0.2721</u>	16.22	0.6664	0.6856	26.00	0.9230	0.2915	14.52	0.8180	0.4057	18.57
	TimeMixer	0.9079	0.2892	13.61	0.8521	0.2733	16.29	0.7923	0.4896	18.47	<u>0.9525</u>	<u>0.2435</u>	<u>12.48</u>	0.8762	0.3239	15.21
	LightTS	0.8896	0.2790	13.63	0.8858	0.2931	16.95	<u>0.8277</u>	<u>0.4474</u>	<u>16.82</u>	0.9433	0.2543	15.20	0.8866	0.3185	15.65
	Crossformer	<b>0.9305</b>	<u>0.2556</u>	<b>12.21</b>	<b>0.9524</b>	0.2874	<u>14.89</u>	0.8213	0.4524	17.08	0.9435	0.2640	13.58	<u>0.9119</u>	<u>0.3149</u>	<u>14.44</u>
	DEFORMTIME	<u>0.9161</u>	<b>0.2437</b>	<u>12.46</u>	<u>0.9356</u>	<b>0.2364</b>	<b>11.69</b>	<b>0.8744</b>	<b>0.3664</b>	<b>13.61</b>	<b>0.9675</b>	<b>0.2023</b>	<b>11.29</b>	<b>0.9234</b>	<b>0.2622</b>	<b>12.26</b>
14	Persistence	0.7572	0.4875	23.00	0.7869	0.3385	19.84	0.6439	0.7283	26.96	0.8239	0.4488	22.49	0.7530	0.5008	23.07
	DLinear	0.7323	0.5767	29.99	0.7371	0.4384	25.44	0.6105	0.6635	27.69	0.8216	0.5085	26.27	0.7254	0.5467	27.35
	PatchTST	0.7626	0.4810	23.33	0.7411	0.3524	21.48	0.6246	0.7164	28.11	0.8102	0.4583	23.44	0.7346	0.5020	24.09
	iTransformer	0.7837	0.4310	20.63	0.7629	0.3448	20.49	0.6138	0.6853	27.21	0.8495	0.4196	21.41	0.7525	0.4702	22.44
	TimeMixer	0.8319	0.3600	17.41	0.8221	0.3153	18.22	0.6668	0.6111	23.48	0.9139	0.3377	17.21	0.8087	0.4060	19.08
	LightTS	0.8697	0.4018	20.65	0.8237	0.3418	20.50	0.7802	0.4999	20.31	<u>0.9366</u>	<u>0.2730</u>	<u>14.70</u>	0.8525	0.3791	19.04
	Crossformer	<u>0.8787</u>	<u>0.3333</u>	<u>16.05</u>	<u>0.8965</u>	<u>0.2980</u>	<u>16.74</u>	<u>0.8339</u>	<u>0.4325</u>	<u>16.91</u>	0.9169	0.3647	19.21	<u>0.8815</u>	<u>0.3571</u>	<u>17.23</u>
	DEFORMTIME	<b>0.9033</b>	<b>0.2962</b>	<b>14.39</b>	<b>0.9374</b>	<b>0.2893</b>	<b>13.15</b>	<b>0.8490</b>	<b>0.3897</b>	<b>14.62</b>	<b>0.9378</b>	<b>0.2584</b>	<b>13.05</b>	<b>0.9069</b>	<b>0.3084</b>	<b>13.80</b>
21	Persistence	0.6682	0.5831	27.54	0.7150	0.4013	23.26	0.5734	0.8466	31.93	0.7520	0.5313	26.92	0.6772	0.5906	27.41
	DLinear	0.6687	0.6032	30.66	0.6920	0.4960	28.49	0.5830	0.7252	30.15	0.7778	0.5760	29.33	0.6804	0.6001	29.66
	PatchTST	0.6899	0.5705	28.41	0.6399	0.4255	26.14	0.5214	0.7963	32.80	0.7137	0.5815	30.27	0.6412	0.5935	29.40
	iTransformer	<u>0.8659</u>	0.3645	17.75	0.7078	0.3702	21.73	0.4561	0.8642	33.94	0.8298	0.4433	23.01	0.7149	0.5106	24.11
	TimeMixer	0.8280	0.4112	19.07	0.8180	<u>0.3058</u>	17.67	0.6555	0.6812	25.45	0.8634	0.4322	23.41	0.7912	0.4576	21.40
	LightTS	0.8354	0.4252	20.19	0.7748	0.4021	25.39	0.6920	0.6201	25.57	0.8699	0.4542	23.80	0.7930	0.4754	23.74
	Crossformer	<b>0.9565</b>	<b>0.3267</b>	<b>15.49</b>	0.8669	0.3168	15.95	<u>0.8777</u>	0.3964	<u>15.11</u>	0.9135	0.3273	<u>17.07</u>	<b>0.9036</b>	<u>0.3418</u>	<u>15.90</u>
	DEFORMTIME	0.8331	<u>0.3543</u>	<u>15.62</u>	<b>0.8966</b>	<b>0.3039</b>	<b>14.99</b>	<b>0.9141</b>	<b>0.3536</b>	<b>13.06</b>	<b>0.9249</b>	<b>0.2598</b>	<b>13.27</b>	<u>0.8922</u>	<b>0.3179</b>	<b>14.24</b>
28	Persistence	0.5763	0.6781	32.15	0.6261	0.4733	27.09	0.5059	0.9541	36.29	0.6705	0.6140	31.14	0.5947	0.6799	31.67
	DLinear	0.6083	0.6496	32.81	0.6016	0.5329	30.18	0.5506	0.7893	32.75	0.7438	0.6539	32.89	0.6261	0.6564	32.16
	PatchTST	0.6067	0.6457	32.75	0.5192	0.4903	30.18	0.4424	0.8809	36.70	0.6555	0.6492	33.78	0.5560	0.6665	33.35
	iTransformer	0.6984	0.5531	27.80	0.5779	0.4444	25.70	0.3211	0.9942	40.08	0.6797	0.6077	30.60	0.5693	0.6498	31.04
	TimeMixer	0.8130	0.4056	21.18	0.8184	<u>0.3244</u>	19.25	0.6444	0.7787	31.60	0.7816	0.5409	24.41	0.7644	0.5124	24.11
	LightTS	0.8462	0.4765	24.49	0.6952	0.4834	25.81	0.7176	0.5616	22.25	<u>0.9037</u>	0.3862	20.33	0.7907	0.4769	23.22
	Crossformer	<b>0.8969</b>	<b>0.3398</b>	<u>16.47</u>	0.8346	0.3647	16.99	<u>0.8514</u>	<u>0.4365</u>	<b>15.42</b>	0.8923	<u>0.3578</u>	<u>16.87</u>	<u>0.8688</u>	<u>0.3747</u>	<u>16.44</u>
	DEFORMTIME	0.8888	<u>0.3718</u>	<b>15.55</b>	<b>0.9046</b>	<b>0.3153</b>	<b>14.57</b>	<b>0.9037</b>	<b>0.4185</b>	<u>16.18</u>	<b>0.9260</b>	<b>0.3069</b>	<b>16.68</b>	<b>0.9058</b>	<b>0.3532</b>	<b>15.74</b>

Instead of projecting the concatenated output of two encoder branches, we take  $\mathbf{Z}_c$  directly from T-DAB as the output  $\mathbf{Z}_j$  of the  $j$ -th encoder layer.

– T-DAB: Denotes that we train a DEFORMTIME model without the T-DAB encoder branch (see section 3.4). We take  $\mathbf{Z}_c$  directly from V-DAB as the output  $\mathbf{Z}_j$  of the  $j$ -th encoder layer.

–  $\mathbf{P}_{v,t}$ : Denotes that we do not use the relative positional biases (both  $\mathbf{P}_v$  and  $\mathbf{P}_t$ ) when obtaining the value embedding for both the V-DAB and T-DAB modules.

– NAE: Denotes that we train a DEFORMTIME model without the NAE module. For an input  $\mathbf{Z} \in \mathbb{R}^{L \times (C+1)}$ , we simply use a fully connected layer to embed the  $C+1$  variables into a hidden dimension of size  $d$  and obtain  $\mathbf{E} \in \mathbb{R}^{L \times d}$ .

–  $\mathbf{P}_n$ : Denotes that we do not use the fixed position embedding  $\mathbf{P}_n$  from the embedding procedure, i.e. instead of Equation 2, we use  $\mathbf{Z}_e = \text{LN}(\mathbf{E})$ .

## D.5 Computational complexity and efficiency of DEFORMTIME – Additional information

The total number of operations (based on multiplications) for DEFORMTIME is given by

$$\underbrace{(C+1)dL+d+2}_{\text{NAE}} \left\{ \underbrace{n \left[ (k^2+1)ld+3ld^2+3\ell^2d+n\ell dL \right]}_{\text{V-DAB}} + \underbrace{r \left[ (k+1)\kappa d+3\kappa d^2+3\kappa^2 d \right]}_{\text{T-DAB}} + 2d+6d^2L \right\} + \underbrace{2d^2L}_{\text{Decoder}} \quad (13)$$

Encoder

Table D4: Seed control (5 seeds) for DEFORMTIME using the ILI-ENG data set across all forecasting horizons ( $H$ ).  $\mu$  and  $\sigma$  denote the mean and standard deviation of the 5 obtained MAEs per test period. The results in the main paper were obtained for seed ‘42’.

$H$	seed	2015/16	2016/17	2017/18	2018/19	Average
7	42	1.379	1.308	2.631	1.248	1.642
	10	1.416	1.063	2.266	1.360	1.526
	111	1.386	0.886	2.315	1.690	1.569
	1111	1.476	1.404	1.986	1.533	1.600
	1234	1.443	1.109	2.197	1.226	1.494
	$\mu$ ( $\sigma$ )	1.42 (0.04)	1.15 (0.18)	2.28 (0.21)	1.41 (0.18)	1.57 (0.06)
14	42	2.056	1.318	3.763	1.786	2.231
	10	1.696	1.514	3.439	1.712	2.090
	111	1.861	1.297	3.556	1.842	2.139
	1111	1.621	1.495	3.327	1.396	1.960
	1234	1.837	1.137	3.879	1.391	2.061
	$\mu$ ( $\sigma$ )	1.81 (0.15)	1.35 (0.14)	3.59 (0.20)	1.63 (0.19)	2.10 (0.10)
21	42	2.170	1.898	4.898	1.633	2.650
	10	2.079	1.507	4.871	1.874	2.583
	111	2.354	1.825	4.668	1.944	2.697
	1111	2.236	1.943	4.158	1.625	2.491
	1234	2.147	1.595	4.406	1.842	2.498
	$\mu$ ( $\sigma$ )	2.20 (0.09)	1.75 (0.17)	4.60 (0.28)	1.78 (0.13)	2.58 (0.09)
28	42	2.654	1.810	4.832	1.595	2.723
	10	2.486	1.692	5.194	1.807	2.795
	111	2.655	1.825	4.887	1.907	2.819
	1111	2.251	1.799	4.529	2.082	2.665
	1234	2.692	1.808	4.939	1.613	2.763
	$\mu$ ( $\sigma$ )	2.55 (0.17)	1.79 (0.05)	4.88 (0.21)	1.80 (0.18)	2.75 (0.06)

The main components that affect the order of operations are the following:

$$\begin{aligned} \text{V-DAB: } \mathcal{V} &= n[(k^2+1)\ell d + 3\ell d^2 + 3\ell^2 d + n\ell d L] \text{ operations} & (14) \\ L \approx n\ell &\implies \mathcal{O}(d^2 L + dL^2) \end{aligned}$$

$$\begin{aligned} \text{T-DAB: } \mathcal{T} &= r[(k+1)\kappa d + 3\kappa d^2 + 3\kappa^2 d] \text{ operations} & (15) \\ L = \kappa r &\implies \mathcal{O}(d^2 L) \end{aligned}$$

$$\begin{aligned} \text{Encoder: } \mathcal{E} &= 2(\mathcal{V} + \mathcal{T} + 2d + 6d^2 L) \text{ operations} & (16) \\ &\implies \mathcal{O}(d^2 L + dL^2) \end{aligned}$$

$$\begin{aligned} \text{Decoder: } \mathcal{G} &= 2d^2 L \text{ operations} & (17) \\ &\implies \mathcal{O}(d^2 L) . \end{aligned}$$

Hence, we conclude that the order of operations for DEFORMTIME is  $\mathcal{O}(d^2 L + dL^2)$ , where  $L$  denotes the length (time steps) of the look-back window, and  $d$  is the size of the hidden layers used throughout our method.

Figure D2 depicts the GPU VRAM memory consumption of DEFORMTIME during training compared to other transformer-based models w.r.t. the length of the look-back window ( $L$ ; part A) and the number of input variables ( $C + 1$ ; part B). In these experiments, we set both the batch size and the hidden dimension  $d$  to 64. While assessing the impact of  $L$ , we set  $C + 1$  to 32, and while assessing the impact of the amount of input variables, we set  $L$  to 56. We then present the average memory consumption across 50 training epochs.

Overall, DEFORMTIME has a relatively small GPU memory footprint. As the length of the look-back window increases (from 28 to 140 time steps), iTransformer (lowest) and DEFORMTIME (second lowest) are showing a stable memory consumption that does not exceed 1 GB. We note that the low memory consumption of iTransformer is expected as it encodes the input over the sequence dimension, i.e. from  $\mathbb{R}^{L \times (C+1)}$  to  $\mathbb{R}^{d \times (C+1)}$ , which guarantees consistent GPU memory usage regardless of the value of  $L$ . In DEFORMTIME, the input partitioning and adaptive transformations within the V-DAB and T-DAB modules reduce computational complexity, leading to reduced memory consumption,

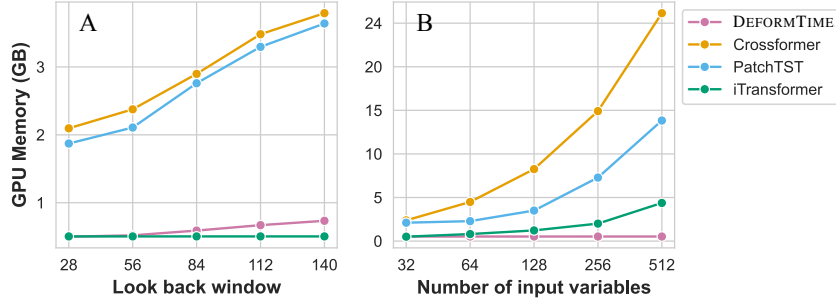


Figure D2: GPU memory (VRAM) consumption based on: (A) the look-back window ( $L$ ), and (B) the number of input variables ( $C+1$ ).

especially when  $L$  is large. At the same time, the memory footprints of PatchTST and Crossformer linearly increase with  $L$ .

As we now increase the number of variables from (32 to 512), other methods display an exponential increase in memory consumption (delayed and considerably lower for iTransformer compared to PatchTST and Crossformer), whereas for DEFORMTIME memory consumption is almost unaffected and stable (e.g.  $< 1$  GB for DEFORMTIME, but  $> 24$  GB for Crossformer). Hence, we argue that our method can handle a greater amount of exogenous predictors more efficiently.

## D.6 A brief note about the performance and evaluation of DLinear

Although DLinear achieved competitive results in prior work [53], the performance drop in our paper originates from the fact that we evaluate models based on their estimate for  $y_{t+H}$ , i.e. the target variable’s value at time step  $t+H$  (see a detailed description of the forecasting task in section 2). In fact, for most tasks this is the target forecast (represented by the corresponding forecasting horizon  $H$ ) and that is what forecasting accuracy should be measured on. Contrary to common sense, DLinear was evaluated on the entire time series (entire sequence of predictions), i.e. from  $y_{t+1}$  to  $y_{t+H}$ . Oddly, this evaluation was conducted in a uniform way, i.e. the error for each time step incurred the same penalty. That may be relevant for some tasks, but it is not relevant to tasks where forecasting  $H$  time steps ahead really necessitates obtaining an accurate forecast  $H$  time steps ahead (and that should be the case for most, if not all, forecasting tasks). DLinear was obviously more accurate in early time steps (lower degree of difficulty), but very inaccurate in later ones (greater degree of difficulty). Hence, in our experiments DLinear displayed the worst forecasting performance.

## D.7 Should MTS forecasting models mix variables in the embedding space?

The paper that presented the PatchTST method [32] provided some empirical evidence for the potential benefits of not modelling inter-variable dependencies. Contrary to that, our results demonstrate that this may not always hold for better models as well as different time series tasks and data sets. Based on our ILI rate forecasting experiments, we deduce that models that mix variables in the embedding space (Crossformer, LightTS, TimeMixer, iTransformer, and DEFORMTIME) outperform the rest. Hence, and perhaps as expected, modelling inter-variable relationships should still be considered a viable approach in time series forecasting.

## E Limitations

In this section, we summarise the potential limitations of this work. As with any machine learning model, the predictive capacity of a forecasting regression function is predominantly determined based on empirical evaluations. To this end, we have conducted extensive experiments. Nevertheless, there are undoubtedly more forecasting tasks that one could use to assess the performance of DEFORMTIME. We have argued about the existence of potential issues within the currently deployed data sets in the evaluation of deep learning forecasters and we have proposed the use of new ones in this paper (alongside some of the previously established benchmarks). Although we hope that we will be able to

share this data set with the broader community, at the time of submission we could only point to the application form for gaining access to the Google Health Trends API that we obtained the data from.

From a qualitative analysis standpoint, it would be interesting to provide further insights about DEFORMTIME's performance under a controlled amount of exogenous predictors. We do make the claim that DEFORMTIME is designed to handle exogenous predictors better and experiment with new data sets that contain significantly more exogenous predictors compared to the established benchmark data sets (and show increased performance gains). However, we do not assess this under a more rigorous experimental design. We could add that our ablation study offers some level of interpretation for the contributions of different components. Nonetheless, further experiments would be required to more concretely understand DEFORMTIME's modelling strengths and weaknesses.

From a methodological perspective, there might be ways to further improve DEFORMTIME. These, of course, could be considered as future avenues of research (as opposed to limitations). First, the deformations we are performing are localised. Perhaps a more expansive deformation approach would be capable of capturing more intricate relationships that a correlation-based neighbourhood omits. In addition, and this applies to all deep learning MTS models, DEFORMTIME does not offer any confidence bounds for its forecasting estimates. We could arguably achieve that via conformal prediction or other approaches. However, how would that affect the accuracy of our mean estimates and the overall model complexity? This is certainly an avenue for follow up work, especially if a forecasting model is to be deployed in practical applications.

## **F Societal impact**

As with any scientific development, our work may have positive but also negative societal impact. From a positive perspective, forecasting models can be used to better predict outcomes in various domains and improve quality of life. Contrary to that, forecasting models could also be exploited by malicious actors in various forms of malpractice. We do think this should be common knowledge. We do also note that there is a thin line between safeguarding AI malpractice and significantly restricting scientific progress (and hence, quality of life improvements). This is beyond the scope of our work and is obviously a broader topic of discussion.

We would like to note that outcomes of this work (e.g. an improved variant of DEFORMTIME) may be used in infectious disease monitoring systems by interested stakeholders (e.g. public health organisations such as CDC, ECDC, UKHSA etc.). These, of course, do not constitute malicious actors. However, a potential risk may arise when (if) a forecasting model provides inaccurate insights. Nevertheless, this is a shared risk among various other disease models (including established mechanistic models). To mitigate this risk, public health agencies use multiple endpoints to determine their course of action (e.g. sentinel and syndromic surveillance, laboratory tests, rapid tests, and vetted epidemiological models). Hence, any decision is based on a collection of different predictors. Nonetheless, prior to the adoption of any forecasting model within public policy, a more thorough and focused (to the said application domain) evaluation of the forecasting method is required.

## **G Supplementary ILI rate forecasting figures**

Here we present a series of figures for the ILI rate forecasting task. Each figure shows the estimates from all models for a certain forecasting horizon and location.



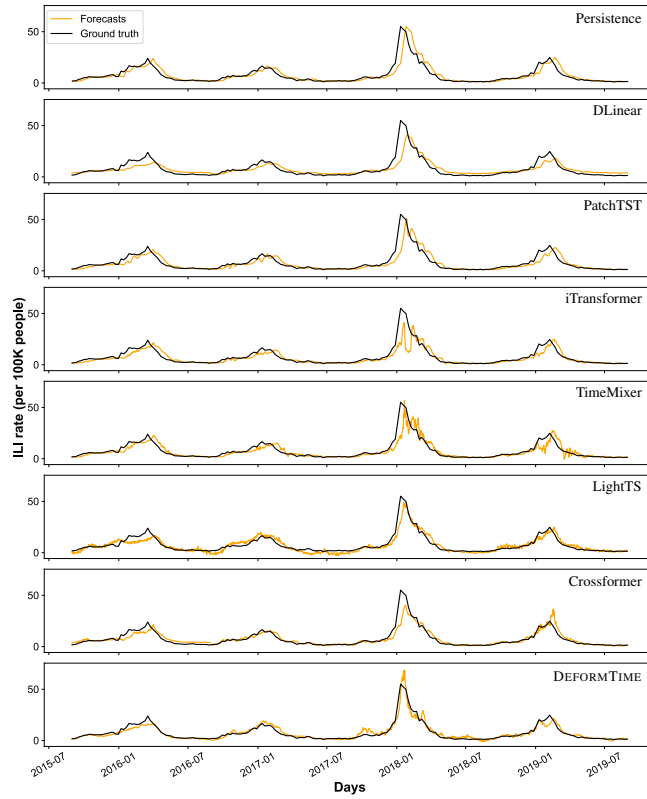


Figure G3: 7 days ahead forecasts for all influenza seasons and models for England (ILI-ENG).

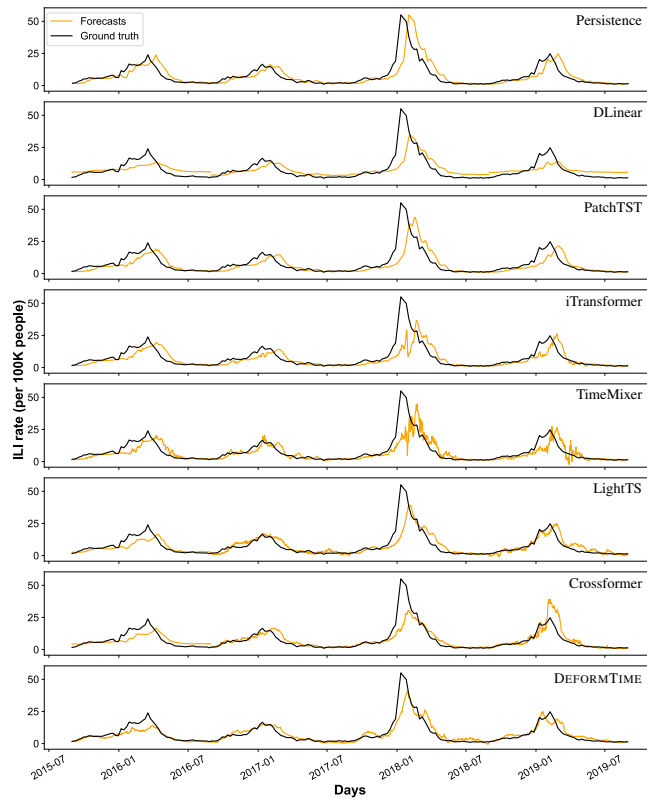


Figure G4: 14 days ahead forecasts for all influenza seasons and models for England (ILI-ENG).

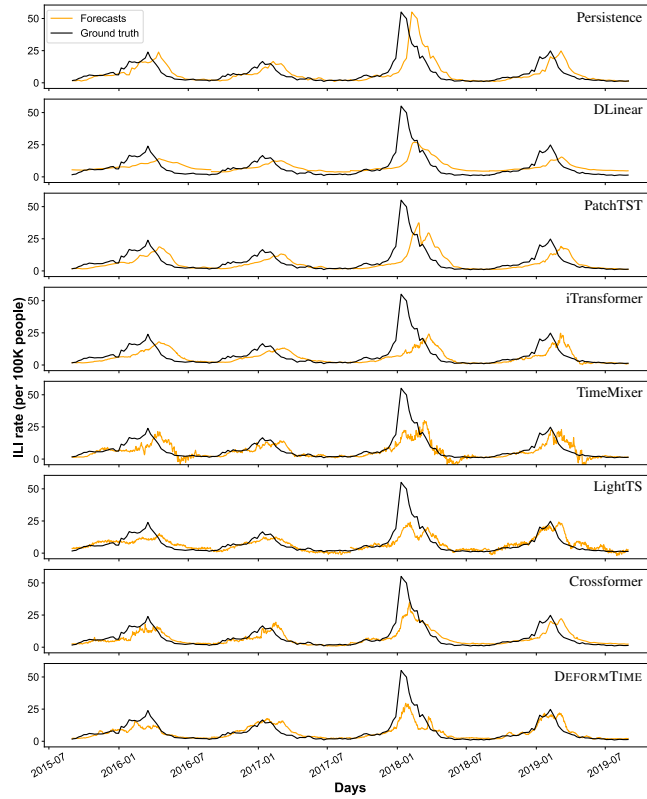


Figure G5: 21 days ahead forecasts for all influenza seasons and models for England (ILI-ENG).

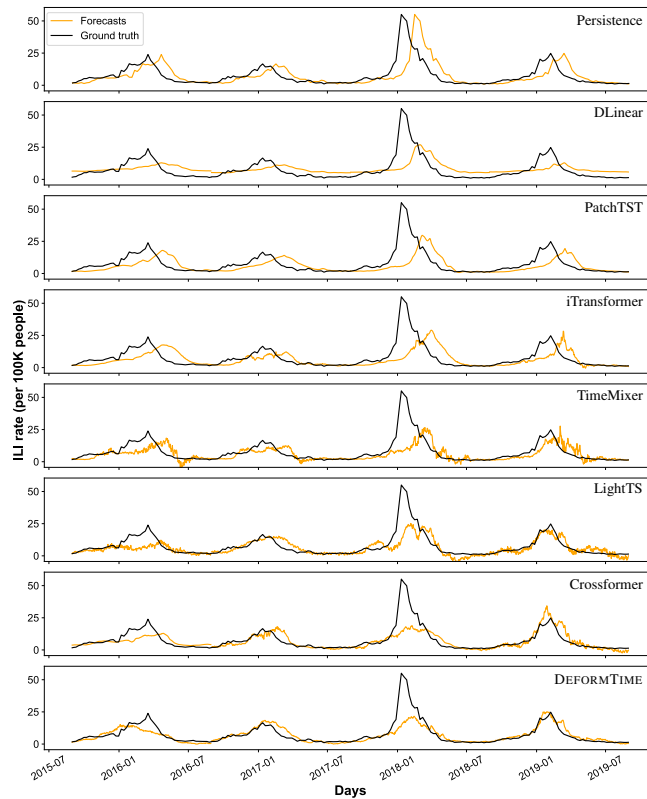


Figure G6: 28 days ahead forecasts for all influenza seasons and models for England (ILI-ENG).

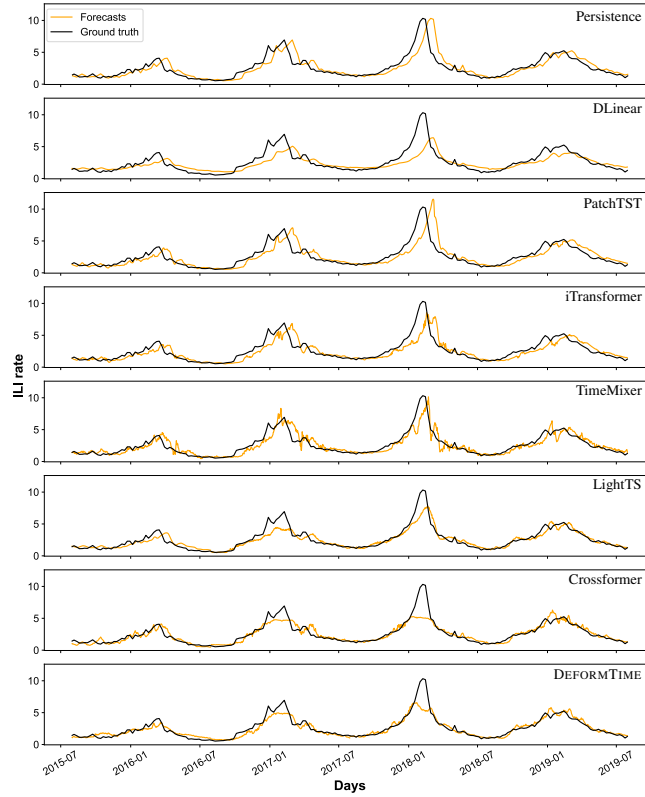


Figure G7: 7 days ahead forecasts for all influenza seasons and models for US Region 2 (ILI-US2).

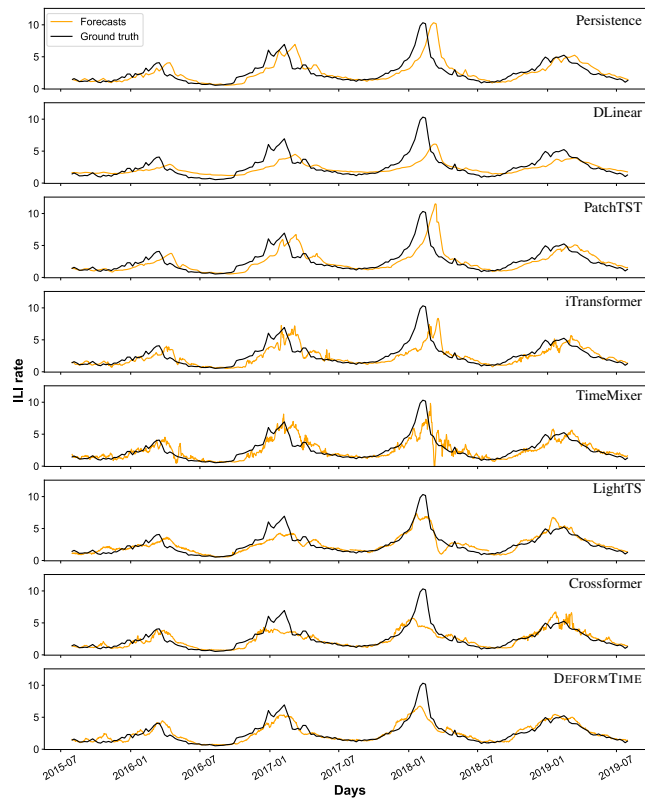


Figure G8: 14 days ahead forecasts for all influenza seasons and models for US Region 2 (ILI-US2).

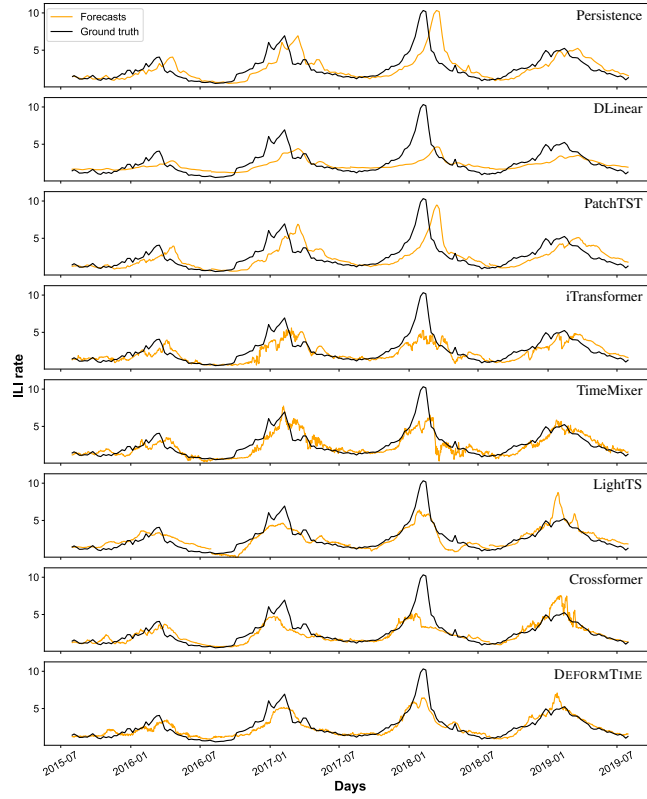


Figure G9: 21 days ahead forecasts for all influenza seasons and models for US Region 2 (ILI-US2).

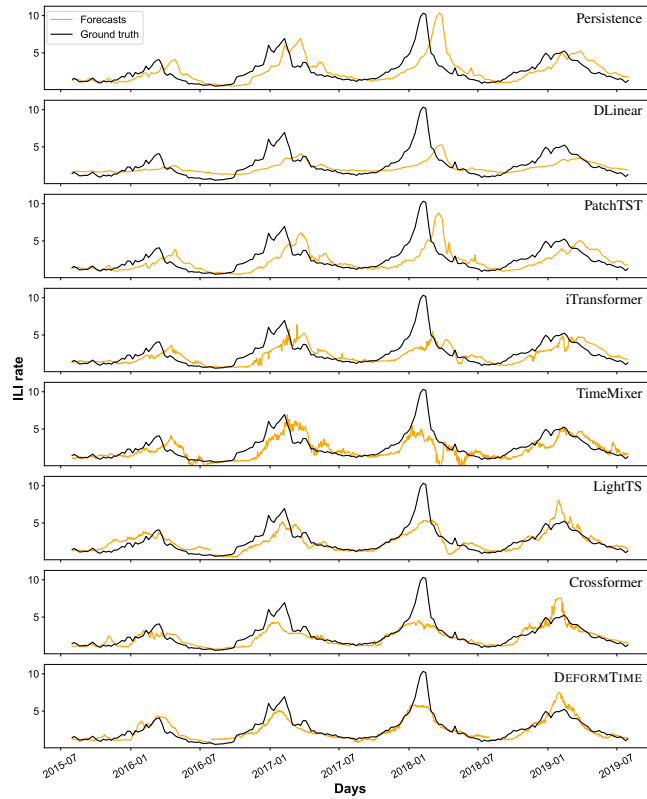


Figure G10: 28 days ahead forecasts for all influenza seasons and models for US Region 2 (ILI-US2).

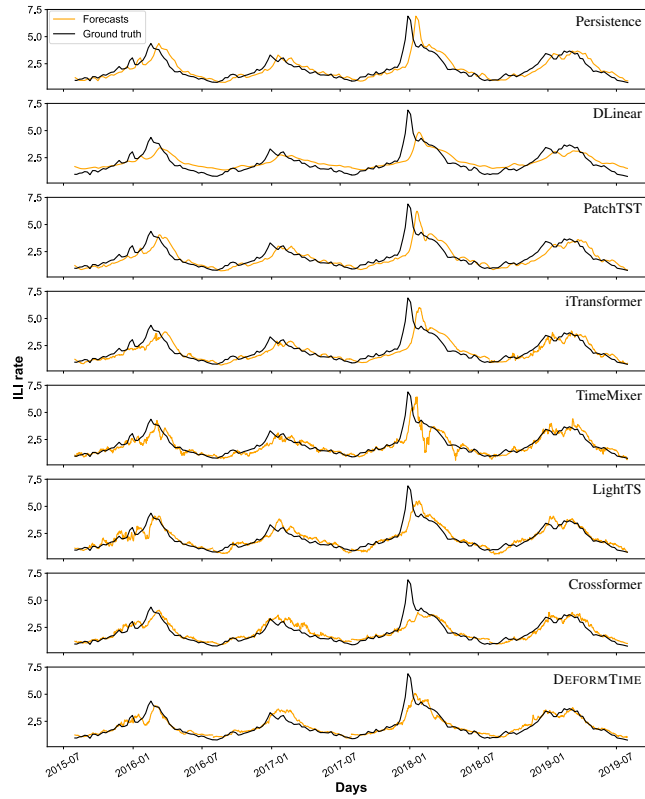


Figure G11: 7 days ahead forecasts for all influenza seasons and models for US Region 9 (ILI-US9).

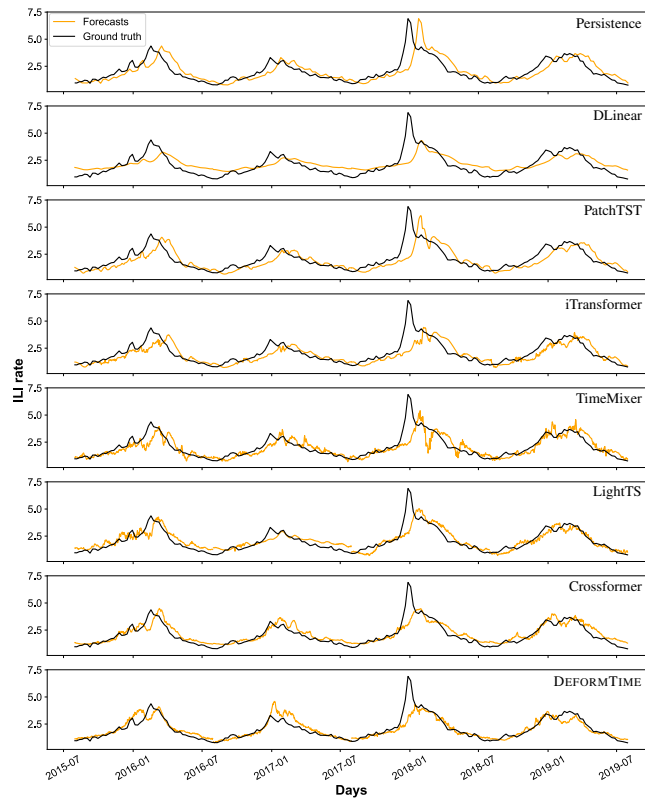


Figure G12: 14 days ahead forecasts for all influenza seasons and models for US Region 9 (ILI-US9).

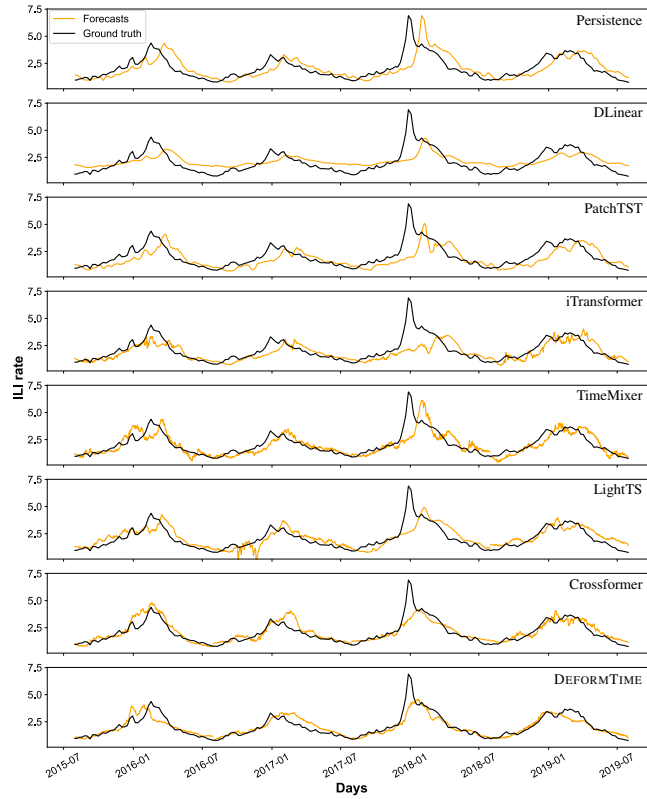


Figure G13: 21 days ahead forecasts for all influenza seasons and models for US Region 9 (ILI-US9).

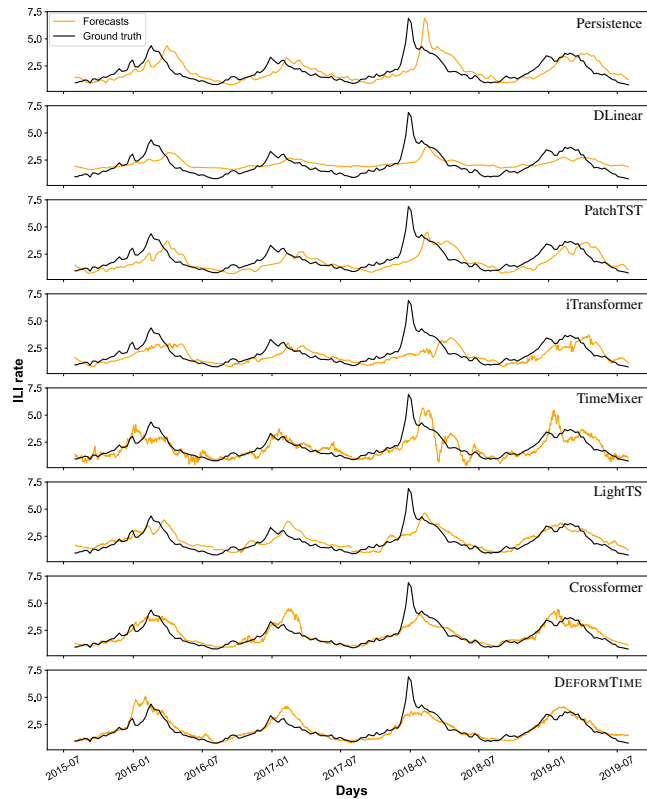


Figure G14: 28 days ahead forecasts for all influenza seasons and models for US Region 9 (ILI-US9).